CHARACTERIZATION OF THE BEHAVIOR OF CONFINED LAMINAR ROUND JETS

by

Douglas Tyler Landfried

Bachelor of Science, University of Pittsburgh, 2009

Submitted to the Graduate Faculty of

Swanson School of Engineering in partial fulfillment

of the requirements for the degree of

Master of Science

University of Pittsburgh

2013

UNIVERSITY OF PITTSBURGH

SWANSON SCHOOL OF ENGINEERING

This thesis was presented

by

Douglas Tyler Landfried

It was defended on

July 12th, 2013

and approved by

Laura Schaefer, PhD., Assistant Professor, Department of Mechanical Engineering and Computer Science, University of Pittsburgh

Anirban Jana, PhD., Senior Scientific Specialist, Pittsburgh Supercomputing Center,

Thesis Advisor: Mark Kimber, PhD., Associate Professor, Department of Mechanical Engineering and Material Science, University of Pittsburgh

CHARACTERIZATION OF THE BEHAVIOR OF CONFINED LAMINAR JETS

Douglas Tyler Landfried, M.S.

University of Pittsburgh, 2013

Laminar jets have been very important in the understanding of fluid dynamics in practical applications. Several examples include expansions in pipes and flow of gas into a large plenum. While much previous research has given consideration to heat transfer behavior and pressure gradients within the confinement, little attention has been paid to quantify the velocity profiles and transitions between various flow regimes. Using a finite volume CFD code, OpenFOAM ®, the incompressible Navier-Stokes equations were solved for a varying expansion ratio, $\psi_{enc} = \frac{r_{enc}}{r_{jet}}$, and varying Reynolds numbers. In the present analysis, three separate Reynolds numbers are tested (Re_{jet}=32.2, 48.3, 64.4, based on the inlet jet diameter and velocity), while the expansion ratio, ψ_{enc}, is varied from 40-100. Results suggest that initially, the flow characteristics are identical to a free jet. At some downstream location, the presence of the enclosure is felt by the jet and deviations begin to be seen from free jet behavior. This transition region continues until at a sufficiently large downstream location, the flow becomes fully developed, internal Poiseuille flow. In this thesis, analysis is conducted for these transition regions and explanations are offered with practical correlations to successfully predict the important flow physics that occur between free jet behavior and Poiseuille flow. Of primary focus are predictive correlations for the jet centerline velocity and the jet half width, as a function of jet Reynolds number and expansion ratio. Similar functional dependence is also

determined for the “linear” decay region of the jet and the reattachment location on the enclosure wall. Key dimensionless parameters are identified, the magnitude of which can be used to classify the flow conditions.

TABLE OF CONTENTS

LIST OF TABLES

LIST OF FIGURES

NOMENCLATURE

ψ_{enc}	Expansion Ratio
A, B	Non-dimensional fit parameters for centerline decay
C, D	Non-dimensional fit parameters for half-width
b	Intercept of free jet centerline velocity
D	Diameter
L_1	Upstream domain length
L_2	Downstream domain length
m	Slope of free jet centerline velocity
p	Pressure
r	Radius
Re	Reynolds Number
$\mathbf{u}$	Velocity vector
U	Velocity Component
x	Axial coordinate
ν	Kinematic viscosity

SUBSCRIPTS

0	$r = 0$, Centerline value
enc	Enclosure
FD	Fully Developed value
jet	Jet Value
lin	Value at deviation from linear
RL	Value at reattachment length
r	Radial component
x	Axial component
vo	Virtual Origin

PREFACE

This research is being performed using funding received from the DOE Office of Nuclear Energy's Nuclear Energy University Programs.

1.0 INTRODUCTION

Jets are commonly found in various natural phenomena and engineering applications, such as volcanic eruptions [1], cooling technologies [2], fuel injectors [3], rocket and jet engine exhausts [4], and nuclear reactors [5]. A significant amount of past literature has focused on free jets that expand into an infinite quiescent medium. These studies have included experimental and analytical investigations on various jet configurations and flow conditions (e.g., laminar as well as turbulent). Seminal works on free jets include those by Bickley [6], Schlichting [7], and Abramovich [8]. However, in actual applications as well as in laboratory experiments, jets are not really free, but are invariably confined by walls to some degree, which may result in flow behavior different from that of the free jet Therefore, it is essential that the flow be understood given the presence of confinement walls and/or obstructions (e.g. tube bundles, impingement plates, etc.).

One particular application where confined jets have practical application is in the lower plenum of next generation (Gen IV) power plants, dubbed Very High Temperature Reactors [9]. In the lower plenum of the Prismatic VHTR, the flow field of which is shown in Figure 1, jets enter the plenum in the vertical direction, before impinging on the bottom of the plenum and turning to flow towards the outlet, shown bottom left. The flow field in the lower plenum is extremely complex, with flows similar to confined jets, impinging jets, and flow across tube bundles, among others. In order to better understand the occurring physics, and increase

validation of computational models, it is necessary to understand the simple flow fields present. One area of interest then, is the flow of confined jets.

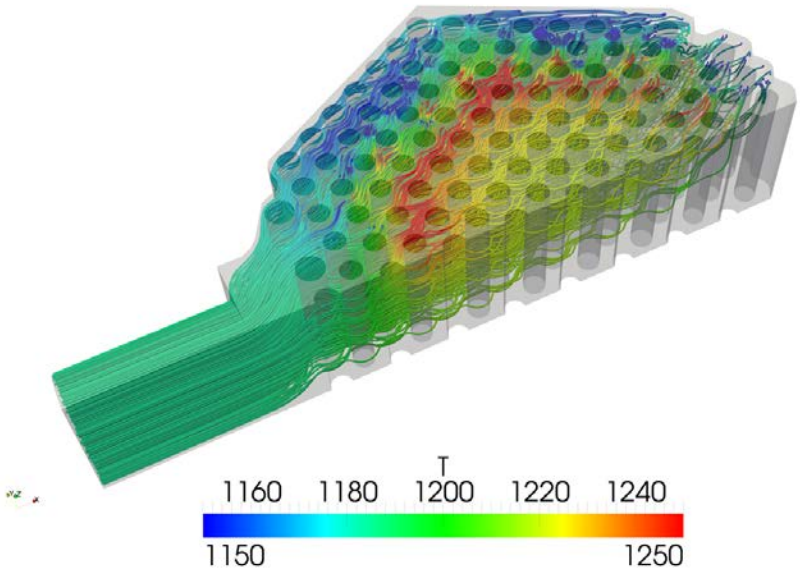

Figure 1 - Half model of VHTR lower plenum: Streamlines overlaid with temperature (In house work)

For axisymmetric flow conditions three distinct types of radial and axial confinement exist, as shown in Figure 2. In Figure 2(a), the confinement is due to lateral walls only. This configuration, which is referred to as a ventilated jet [10], allows unrestricted entrainment of the fluid upstream of the jet nozzle. The flow rate downstream includes that due to both the jet and the secondary flow. Two other confinement types are shown in Figure 2(b) and 1(c), where the entrainment of fluid upstream of the jet nozzle is restricted by the presence of a back wall, causing both to have regions of significant recirculation. The difference between these two is the location of the back wall. Figure 2(b) illustrates the case where the jet nozzle is flush with the back wall. In Figure 2(c) on the other hand, the back wall is located far enough upstream of the jet nozzle as to not affect the jet flow downstream of the inlet. In all cases, as the size of the

enclosure approaches infinity, the flow field of the jet would approach that of a free jet in a quiescent medium.

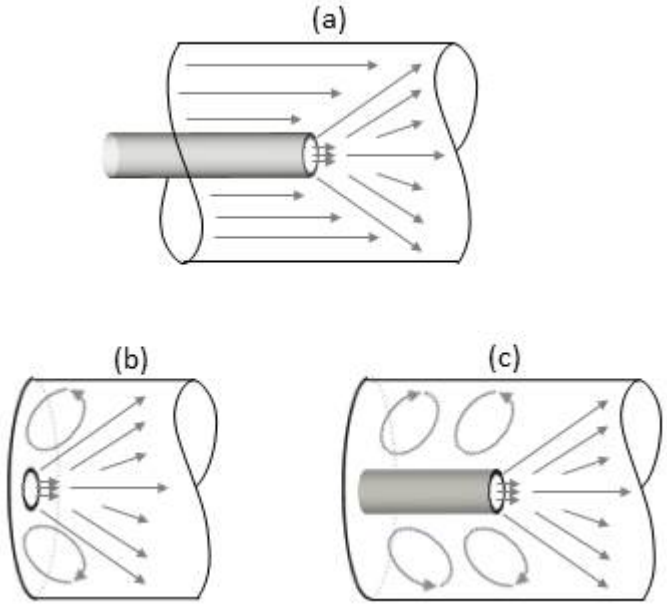

Figure 2 - Various confined jets: (a) Laterally confined only, no back wall, (b) Jet inlet flush with back wall, (c) Jet inlet downstream of back wall

In this thesis, a careful numerical investigation is performed focusing on the effects of a confinement, as illustrated in Figure 2(c). The flow field from a laminar round jet is studied as a function of two non-dimensional numbers: (i) the expansion ratio $\left(40 \le \psi_{enc} \le 100\right)$ and (ii) the jet Reynolds number ($\mathrm{Re}_{enc} = \dfrac{U_{jet} D_{jet}}{\nu} =$ 32.2, 48.3, and 64.4). Qualitative flow regimes are first identified, as well as the transition regions between them. Of particular importance is quantifying the downstream location where the flow behavior begins to feel the presence of the enclosure walls and deviates from free jet predictions. While some previous mathematical analyses [11] have investigated flow behavior, they have not presented compact correlations to predict the flow, while other experimental investigations [12] did not investigate large expansion ratios. The

transition regions identified in this work include the location where the jet begins to deviate from the linear behavior associated with a free jet, the location where the flow reattaches to the confinement wall, known as the reattachment length, and the location where flow in the confinement becomes fully developed. Finally, correlations are developed to capture the dependence of the centerline velocity and jet half width on Reynolds number and enclosure size.

The remainder of the thesis is organized as follows: Chapter 2.0 summarizes the literature on the behavior of free and confined laminar round jets; Chapter 3.0 describes the computational model and the procedure for obtaining results; Chapter 4.0 describes the flow regimes and transitions; Chapter 5.0 establishes correlations for the centerline velocity and jet half width; Chapter 6.0 summarizes the main conclusions of this study.

2.0 BACKGROUND

2.1 FREE JET BEHAVIOR

The first fundamental benchmark for describing jet behavior is the analytical solution for a laminar jet issuing into an infinite quiescent medium, i.e., the free jet. As shown by Schlichting [13], and later by Pai [14], boundary layer theory can be used to analytically solve the Navier-Stokes equations for the velocity field in an incompressible, axisymmetric round free jet. This solution, which mimicked flow from a point momentum source, had good agreement with experimental results at locations sufficiently far from the outlet such that a self-similar solution could be assumed. For the free laminar round jet, power law relationships for the centerline velocity and the spreading rate of the jet half width were found with respect to the axial coordinate, x.

In the analytical solution, the jet was assumed to be issuing from a point momentum source, the jet momentum flux was constant, and the jet mass flux increased downstream, due to entrainment. However, a point momentum source is unable to accurately describe the flow behavior for a real jet (i.e., finite diameter jet with potential core flow signatures), especially near the jet nozzle. This necessitates a first order correction of the free jet equations, which was first experimentally quantified by Andrade & Tsien [15], while an analytical approach to this problem was conducted much later by Revuelta et al. [16]. In this correction, the point-source location of

the jet is shifted some distance $\left(x_{vo}\right)$, upstream of the jet exit. This accommodation is known as the virtual origin. For a top hat (i.e. uniform) inlet velocity profile, Revuelta et al. [16] found the virtual origin to be $x_{vo} = 0.0575 D_{jet}$.

Incorporating the virtual origin into Schlichting's solution [13], expressions for the centerline velocity decay, $\frac{U_{jet}}{U_0\left(x/D_{jet}\right)}$, and the jet half width, $\frac{r_{1/2}\left(x/D_{jet}\right)}{r_{jet}}$, can be found according to:

$$\frac{U_{jet}\left(x/D_{jet}\right)}{U_0} = \frac{32}{3\mathrm{Re}_{jet}}\left(\frac{x - x_{vo}}{D_{jet}}\right) \tag{2.1}$$

$$\frac{r_{1/2}\left(x/D_{jet}\right)}{r_{jet}} = \frac{32}{3\mathrm{Re}_{jet}}\sqrt{\frac{\sqrt{2}-1}{3}}\left(\frac{x - x_{vo}}{D_{jet}}\right) \tag{2.2}$$

2.2 CONFINED ROUND JETS

The effect of confinement on jet behavior may be significant even if the walls are far away. For these studies, the behavior is very much dependent on the enclosure size, quantified by the expansion ratio. As the expansion ratio approaches infinity, conditions more closely resemble those of a free jet. Sarma et al. [17] numerically investigated the effects of Reynolds number and expansion ratio on the flow field in a two dimensional laminar slot jet with both recirculating and non-recirculating boundary conditions in transitional flow regimes. It was observed that for non-entraining boundary conditions (similar to the round jet case shown in Figure 2(b)), the flow develops lateral oscillations in the velocity field for moderate expansion

ratios $\left(4 \le \psi_{enc} \le 20\right)$. However, since plane jets do not decay and spread at the same rate as round jets, the conclusions reached in that study are not entirely applicable to the current focus of laminar round jets. Similar experimental work was carried out to investigate a sudden, axisymmetric expansion. A particle image velocimetry study (PIV) of flow in a round, sudden expansion with $20 \le \mathrm{Re}_{jet} \le 211$ was carried out by Hammad et al. [12]. During the study, special consideration was given to both radial profiles of velocity and contour plots of the stream function. However, while correlations were developed for the recirculation length as a function of Reynolds number, the study examined only a small expansion ratio, $\psi_{enc} = 2$. Additional studies on laminar confined jets include the experimental work by Iribarne et al. [18], who studied an axisymmetric pipe jet with an expansion ratio of $\psi_{enc} = 2$. Using instantaneous flow visualization techniques, they investigated mean velocity profiles, shear stresses and reattachment lengths. Additionally, they found that the Nusselt number, in heated flow experiments, increased up to the reattachment length. A similar experimental investigation of confined round jets was carried out by Back & Roschke [19], where the jet Reynolds number was varied from 20-4200 to investigate reattachment length as a function of step height. Also investigated were instabilities in the flow and transitions between laminar flow, development of stable waves, and fully turbulent behavior. For that study, dye injection along the wall was used to determine the reattachment length, while a separate dye injection in the main flow of the jet was used to determine the flow stability. For low Reynolds number flows, it was shown from mixing theory that the reattachment length, varied linearly with Reynolds number.

Other common scenarios worth considering are flow over a sudden expansion and flow over a backward facing step. Durst et al. [20] further carried out an extensive experimental and theoretical study of flow in a sudden expansion. Reynolds numbers of 70, 300, and 610 were

studied. Special care was given to determine reattachment lengths on both confinement walls, as well as steady-state transitions in the flow, as a function of Reynolds Number. However, only one expansion ratio, $\psi_{enc} = 2$ and one Reynolds number in the laminar range (i.e. $\mathrm{Re}_{jet} < 100$) were studied. Armaly et al. [21] carried out theoretical and experimental studies of flow over a back-ward facing step, which is similar qualitatively to flow over in a sudden expansion. For a fixed expansion ratio of 1.94, the Reynolds number was varied from 70-8000. While the theoretical results assumed 2D flow, strong 3D flow characteristics were observed, especially near the corners of the backward facing step. Similarly, a study by Alleborn et al. [22] investigated the linear stability of a sudden expansion in 2D flow and the dependence of the flow on the Reynolds number and confinement size. Although a rigorous mathematical analysis was conducted, little attention was given to actually determining physical flow features, such as reattachment length. For high Reynolds numbers, Acrivos & Schrader [23] studied a sudden expansion with both parabolic and uniform inlet velocity profiles. Special attention was given to simplifying the Navier-Stokes equations in all important flow regions. Additionally, it was found that for both conditions, the reattachment length varied linearly with Re_{jet} up to $O(10^2)$. However, effort was not made to solve the complete Navier-Stokes equations, only the reduced term approximations.

For the free and confined round turbulent jets, List [24] and Ball et al. [25] both have conducted extensive reviews of work in the field. Included in the review by List [24] are previous works on free round jets, free plane jets, buoyant plumes, and jets with the presence of cross flow and stratifications. The review of Ball [25] focuses on turbulent jets, with special notes on history while detailing previous work, including analytic experimental, and computational work, such as RANS, LES, and DNS. Two significant attempts have been made

to characterize the effects of confinement on turbulent jets. First, Kandakure et al. [26] utilized a $k - \omega$ turbulence model to simulate confined jet flow. The centerline velocity profile, and the jet half-width, and the Reynolds stresses were plotted as functions of downstream location for expansion ratios ranging from 6 to 50. These results were found to be in good agreement with the experimental results of Hussein et al. [27], who studied the effects of confinement on free-jet behavior with special attention given to quantifying how the experimental errors present in hot-wire anemometry measurements did not satisfy the balance of linear momentum equations. Similar work was carried out by Panchapakesan & Lumley [28] for a round jet of air, and in Panchapakesan & Lumley [29] for a round jet of helium. Although much insight has been achieved in regard to both laminar free and confined jets, these advances have largely been qualitative with only limited information being reported about the velocity field. There is a need for a set of predictive correlations for centerline velocity, half width, reattachment length, and transition regions within the flow, as well as an understanding of the effects of the enclosure on these parameters., which is a first step in ultimately characterizing more complex jet configurations and confinement types.

3.0 COMPUTATIONAL METHODOLOGY

3.1 DOMAIN AND MESH DESIGN

In this paper, behavior of confined, round, laminar jets was studied computationally using the open source, collocated, finite volume, Computational Fluid Dynamics (CFD) package OpenFOAM ® [30]. Specifically, the simpleFoam solver available in OpenFOAM ® was used to solve the steady state, incompressible Navier-Stokes equations, shown in Eqs. 3.1 and 3.2, for mass and linear momentum conservation on an axisymmetric domain, to obtain the time-independent velocity field $\mathbf{u} = U_x(x,r)\mathbf{e_x} + U_r(x,r)\mathbf{e_r}$ and pressure field $p(x,r)$ for the laminar jet. Equation 3.1, the divergence of the velocity field, represents the necessary and sufficient condition to insure conservation of mass for an incompressible flow field with constant density. Similarly, for incompressible flow, Eq. 3.2 consists of a non-linear convective term on the right hand side, while on the left hand side a laplacian of the velocity field accounts for viscous diffusion and a gradient of pressure represents the gradient of the spherical component of the stress tensor which causes acceleration of the fluid down the gradient. The simpleFoam algorithm is an implementation of the finite-volume based Semi-IMplicit Pressure Linked Equation (SIMPLE) algorithm originally developed by Patankar & Spalding [31]. The SIMPLE algorithm, a standard steady state algorithm already implemented in OpenFOAM ®, is described in Chapter 3.1.1. For details of the implementation of this algorithm in OpenFOAM ® see, for

example, Jasak [32]. In the Chapters that follow, more details of the computation methodology is provided.

$$\nabla \bullet \mathbf{u} = 0 \tag{3.1}$$

$$\mathbf{u} \bullet \nabla \mathbf{u} = \frac{-1}{\rho} \nabla p + \nu \nabla^2 \mathbf{u} \tag{3.2}$$

In order to reduce computational time, the flow is assumed to be axisymmetric about the common centerline of the jet and confinement. This standard 2-D axisymmetric analysis is achieved in OpenFOAM ® through implementing "wedge" boundary conditions. This essentially analyzes a thin slice of the domain as illustrated in Figure 3. To accommodate mass flow through the lateral sides of the elements, a periodic boundary condition is applied.

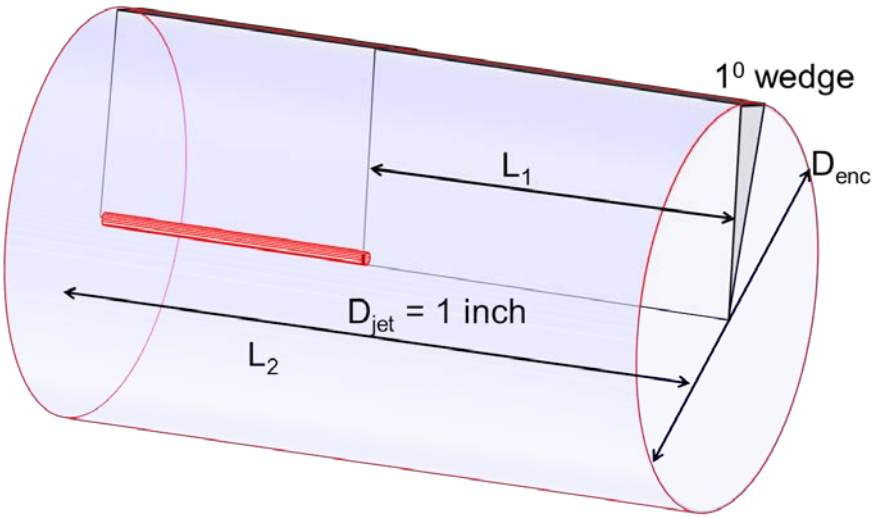

Figure 3 - Illustration of sliver domain, overlaid circular domain

To aid in mesh design, preliminary studies were conducted on a very coarse uniform mesh for the purpose of determining key flow characteristics and the effects of various geometric constraints, such as upstream and downstream length, on the flow. An overview of these studies is given in Chapter A.3.1. From these studies, the mesh was designed as shown in Figure 4.

Radially, within $21r_{jet}$ of the centerline a fine uniform mesh was employed because this region corresponds to the spreading of the jet shear layer. The radial element size in this region is 8 elements per jet radius. Beyond the shear layer, in the radial direction from $21r_{jet}$ out to $(\psi_{end} - 10)r_{jet}$ is the recirculation region where the large mixing eddy occurs. In this region the mesh expands for half the distance, then contracts for half the distance. For both expansion and the contraction, the number of elements was selected such that the largest expansion, or contraction, was only 5% between consecutive cells. Beyond the contracting region, approaching the wall, is a uniform mesh with 8 radial elements per jet radius. Several additional considerations were made when considering the design of the mesh in the axial direction. First, the grading in the axial direction, both upstream and downstream, defined as the ratio of the length of the last cell to the length of the first cell, was 2. In all cases the upstream axial length was $48r_{jet}$, with 547 elements in the axial direction.

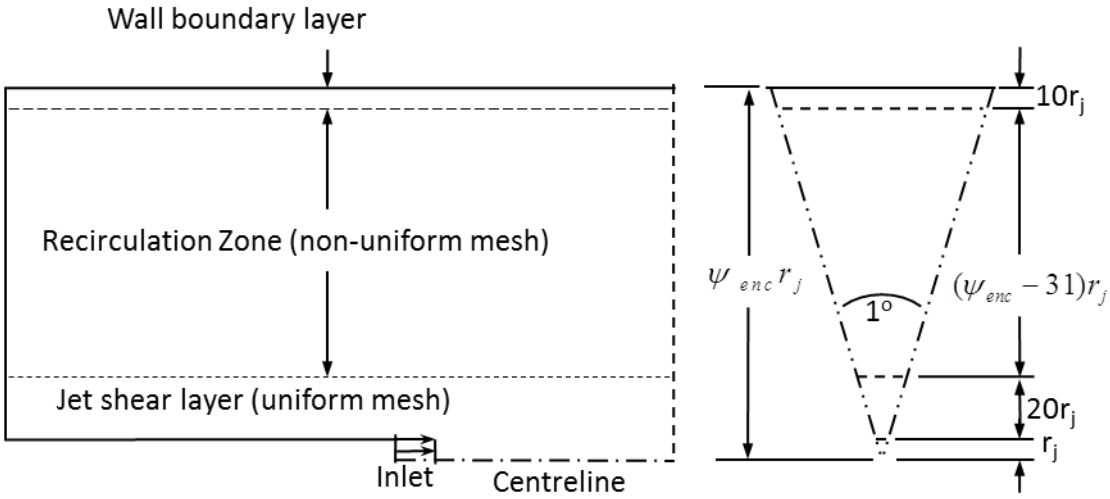

Figure 4 - Schematic of computational domain for axisymmetric simulation

The downstream length was selected uniquely based on the coarse mesh studies, such that the outlet occurred downstream of the onset of Hagen-Poiseuille, fully developed flow [33]. The

number of elements in the axial direction was scaled in each case, based on the length, such that there were 2000 elements in a 14m domain (i.e., for $\psi_{enc} = 80$, L = 6m with 820 elements). A discussion of why this mesh resolution was selected is included later in Chapter 3.2. The boundary conditions applied to the domain are listed in Table 1. As shown, a uniform "top-hat" velocity profile was applied at the jet inlet, whose magnitude $\left(U_{jet}\right)$ was varied to achieve the desired jet Reynolds number. A standard no-slip condition was applied to all wall boundaries including the enclosure wall and the outer surface of the pipe delivering the jet into the domain. Finally, at the outlet of the enclosure the gradient of velocity was set to zero, while the gradient of pressure was calculated for fully developed Poiseuille flow [33]. Since pressure was never specified anywhere, a reference pressure of 0 was set at the inlet of the jet. The tolerance on **u** and *p* was set to 10^{-9}. Additionally, the relaxation factor was set to 0.5 for **u** and 0.7 for *p*. Gauss linear discretization, a central difference second order integration scheme, was used for numerical discretization of all terms, including gradients, divergence, laplacians, and interpolations. Since only a steady state solution was desired, a steady state time scheme, $\frac{\partial \mathbf{u}}{\partial t} = 0$, was used. These are discussed more in appendix A.3.1.

Table 1 - Boundary Conditions applied to simulation domain

Boundary	Velocity	Pressure
Inlet	$\mathbf{u} = U_{jet}\mathbf{e_x}$	$\frac{\partial p}{\partial x} = 0$
Walls	$\mathbf{u} = \mathbf{0}$	$\frac{\partial p}{\partial \mathbf{n}} = 0$
Outlet	$\frac{\partial \mathbf{u}}{\partial x} = 0$	$\frac{\partial p}{\partial x} = \frac{8\mu U_{jet}}{\psi_{enc}^4 r_{jet}^2}$

For the simulations, a range of Reynolds numbers, $\mathrm{Re}_{jet} = [32.2,\ 48.3,\ 64.4]$, and expansion ratios, $\psi_{enc} = [40, 50, 60, 70, 80, 90, 100]$ were studied. The radius of the jet was fixed for all cases ($r_{jet} = 0.01\mathrm{m}$). Therefore, in order to vary the Reynolds number, the magnitude of the top hat velocity profile, U_{jet}, was varied. The top hat, uniform velocity profile is shown in Figure 4. The fluid was assumed to be air, with a kinematic viscosity $\nu = 15.68 \cdot 10^{-6} \frac{m^2}{s}$.

3.1.1 The SIMPLE algorithm

The Semi-IMplicit Pressure LinkEd algorithm, SIMPLE, developed by Patankar [31], is an iterative solution procedure for solving the steady state Navier-Stokes equations for balance of linear momentum (Eq. (3.2)). The solution method takes advantage of the fact that it possible to decouple the linear velocity-pressure relation when changes are large. It is assumed that pressure and velocity can be written as shown in Eqs. 3.3 and 3.4 respectively, where the prime (') denotes a correction and the subscript ($_0$) denotes the original guess, or the value from the previous time step. Substituting Eqs. 3.3 and 3.4 into the momentum equation, neglecting non-linear terms and accounting for conservation of mass (Eq. 3.1), a equation for velocity correction, Eq. 3.5, and a *pressure correction equation*, Eq. 3.6, are derived. Note in Eq. 3.6 that *A* is a fictitious time increment divided by the density of the fluid. The value for *p'* is then used in Eq. 3.3 to correct the pressure.

$$p = p_0 + p' \tag{3.3}$$

$$\mathbf{u} = \mathbf{u}_0 + \mathbf{u}' \tag{3.4}$$

$$\mathbf{u}' = A\frac{\partial p'}{\partial \mathbf{x}} \tag{3.5}$$

$$\nabla^2 p' = \frac{1}{A}\left(\nabla \bullet \mathbf{u}_0\right) \tag{3.6}$$

At the start of the SIMPLE algorithm, an approximate solution of the momentum equation (Eq. 3.2) is calculated using the initial values set for pressure. At this step the solution is under-relaxed. In OpenFOAM ® the under-relaxation is done using an implicit method which enhances diagonalization of the matrix equations corresponding to the domain. A pressure correction and momentum correction are applied. After the pressure is corrected, it is under-relaxed according to Eq. 3.7, which is a modification of the original equation for pressure (Eq. (3.3)). Note that the under-relaxation factor, α, varies from 0 to 1, with 0 corresponding to no change in the pressure, and 1 being the pressure equation given in Eq. 3.3. The momentum corrector is applied as shown in Eq.3.5. After the pressure and momentum correctors have been applied, the process is repeated, starting with recalculating velocities based on the new pressure.

$$p^{new} = p_0 + \alpha\left(p'\right) \tag{3.7}$$

3.2 CONVERGENCE CRITERION

Several issues were addressed relating to the accuracy of the solution. First, it was necessary to establish criteria to determine when the solution had become converged. Second, it was necessary to determine the accuracy of a particular mesh. This was done by utilizing the grid convergence index (GCI), a modified version of the Richardson Extrapolation [34].

One common practice in determining the iterative convergence of a solution is to monitor the residuals, normally defined as the L_1 norm of each variable investigated. However, if convergence is identified by monitoring when the residuals fall below a certain level, the data may appear converged even when small changes are occurring. Thus, in order to determine iterative convergence, three specific locations in the domain were monitored. These locations are: (i) 60 diameters downstream $\left(x = 60D_{jet}\right)$ where the centerline velocity was monitored, (ii) the reattachment length $\left(x_{RL}\right)$ and the centerline velocity at that axial location, and (iii) location where fully developed internal flow conditions are achieved $\left(x_{FD}\right)$ and the axial velocity at the location. Convergence was defined to occur when all of the tracked quantities varied by less than 0.5% between subsequent iterations. All cases were decomposed in parallel and run on 32 cores for several weeks before convergence criteria were met.

It should be noted that since the centerline of the jet falls on the edge of the first row of cells, it was necessary to extrapolate the cell centered data to the centerline in the domain for all three parameters used to evaluate convergence. Additional analysis periodically requires assessing other velocities which often do not exist at cell center locations. All extrapolation and interpolation was performed utilizing a standard cubic fit which used raw data for all cells at the nearest four cell centers in both the axial and radial direction.

After establishing iterative convergence criteria, the spatial discretization error was quantified, using the concept of Grid Convergence Index (GCI) [34]. The Grid Convergence Index study allows for an uncertainty, due to the mesh refinement level, to be placed on any relevant data. However, one drawback of GCI is the need for multiple grid refinements for comparison. In the current study, meshes accounting for both axial and radial refinements, were ran on a fixed case, $\psi_{enc} = 80$ and $\mathrm{Re}_{jet} = 32.2$. Grid Convergence Index assumes the error of

the solution is in the asymptotic region, namely that the error decreases as a function of the local mesh scale according to Eq. 3.8, where ε is the error, *h* is the local length scale, and *p* is the order of the discretization method used. For the present study the local length scale was defined as the cube root of volume of the cell containing the particular point of interest.

$$\varepsilon \propto h^p \tag{3.8}$$

First, important quantities such as the centerline velocity at a specific axial location, are selected as the studied parameter ϕ. After ϕ has been selected, the three unique meshes are then compared to determine the uncertainty associated with the solution. Next, the error between two different meshes is calculated. Note that for all equations relating to GCI, any two number subscript represents the difference between two cases: i.e. $\varepsilon_{32} = \phi_3 - \phi_2$. After determining the error, the local refinement between the two cases is calculated as $r_{21} = \frac{h_2}{h_1}$. When referring to the different meshes it is assumed that for the number of elements, N_i, $N_1 > N_2 > N_3$ and that $h_1 < h_2 < h_3$ accordingly. Next, the apparent order of the discretization method is calculated according to Eq. 3.9, where $s = \text{sgn}\left(\frac{\varepsilon_{32}}{\varepsilon_{21}}\right)$. A negative value of *s* suggests oscillatory convergence is occurring at that particular location. As shown, *p* must be determined using an iterative method.

$$p = \frac{1}{\ln\left(r_{21}\right)}\left|\ln\left|\frac{\varepsilon_{32}}{\varepsilon_{21}}\right| + \ln\left(\frac{r_{21}^p - s}{r_{32}^p - s}\right)\right| \tag{3.9}$$

Finally, once the apparent order is known, the GCI for the refined mesh can be calculated according to Eq. 3.10, where FS is a factor of safety tied to the fact that it is unknown whether

the solution is truly in the asymptotic region. For the present work, the factor of safety used was 1.25, as suggested by Celik [35].

$$GCI_{21} = \frac{FS}{r_{21}^{p} - 1}\left|\frac{\phi_1 - \phi_2}{\phi_1}\right| \tag{3.10}$$

The total number of finite volume cells for the three meshes utilized was 82634, 169384, and 454936. In order to quantify the GCI for the entire domain, a uniform sampling of velocities was used in both the axial and radial directions. In the axial direction, 80 evenly spaced points were sampled for $\frac{x}{D_{jet}}$ between 0 and 200, while in the radial direction 40 evenly spaced points were sampled from $\frac{r}{r_{jet}}$ = 0 to 80, for a total of 3200 sampled points. For each of the three meshes under investigation, knowledge of the cell size at these sampling locations and the two component velocity vector enables calculation of the GCI. The result for axial velocity, quantified as the percent uncertainty, is illustrated in Figure 5(a). This is presented along with the streamlines of the data in order to qualitatively understand the uncertainty in terms of the velocity field. As shown, the band with the largest percent uncertainty propagates from the reattachment point, downward through the recirculation center, and then toward the edge of the jet inlet. It should be noted that along this band, the flow has almost no component of velocity in the axial direction, therefore, a large percent uncertainty does not imply a large uncertainty in the actual velocity. Considering the distribution of the GCI data shown in Figure 5(a), it was found that 95% of the locations sampled had an uncertainty of less than 41.25%. Moreover, 75.91% of the data points had less than a 5% error, while 55.31% had an uncertainty of less than 2.5%. The average GCI for the entire domain, when considering U_x only, was 5.65%. Additionally, shown in Figure 5(b), is the GCI for U_r. Considering the distribution of the GCI for U_r, 98% of the

data has an uncertainty of less than 15%. Moreover, 69.7%% of the data has an uncertainty of less than 5%. The average GCI for the radial velocity is 4.15%. Note that for both Figure 5(a) and (b), any error larger than 15% is shown at the maximum displayed value, to increase clarity which is otherwise distorted by excessively large values related to the use of relative error instead of absolute error.

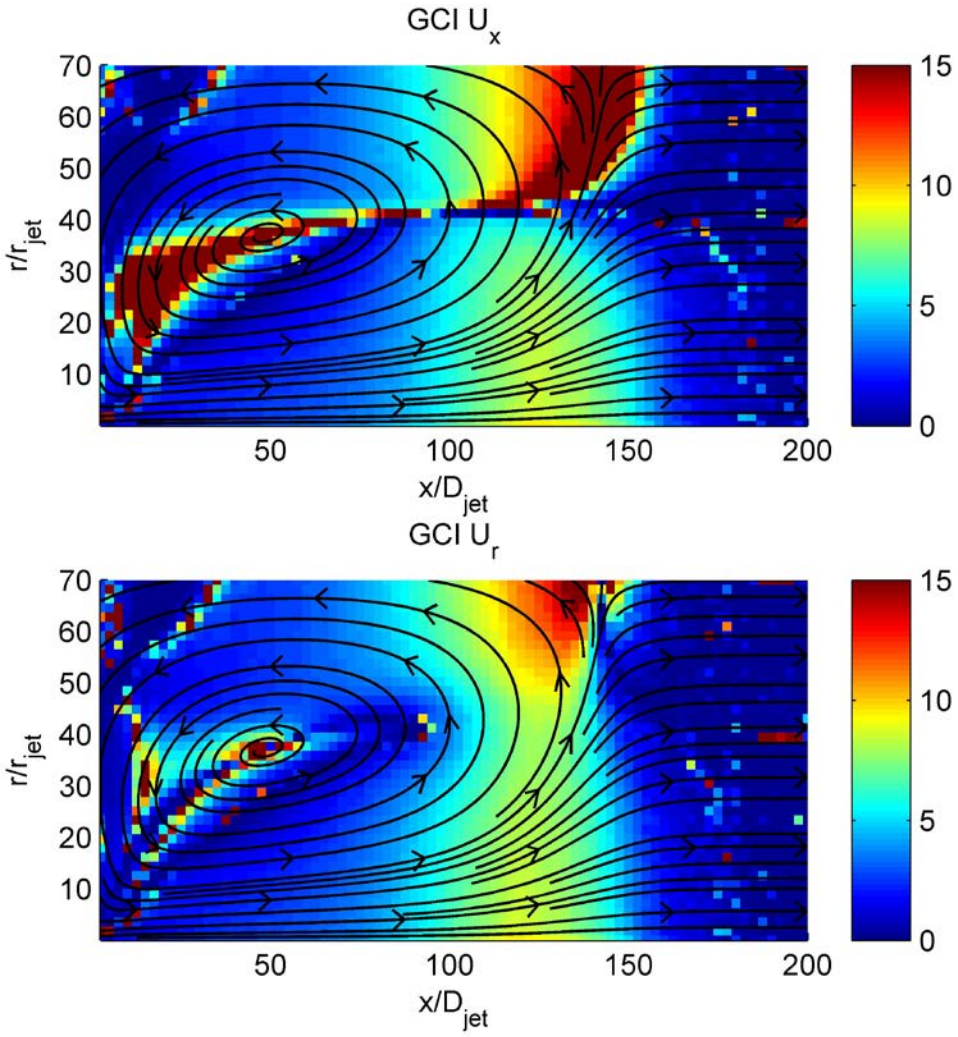

Figure 5 - (a) %GCI for U_x overlaid with flow Streamlines for $\psi_{enc} = 80$ and $\mathrm{Re}_{jet} = 32.2$

(b) %GCI for U_r overlaid with flow Streamlines for $\psi_{enc} = 80$ and $\mathrm{Re}_{jet} = 32.2$

Since both U_x and U_r contribute to the velocity field, additional studies were conducted, where the variables examined were both functions of U_x and U_r. Accordingly, the GCI was studied for both magnitude, $|\mathbf{u}| = \sqrt{U_x^2 + U_r^2}$, and direction, $\theta = \arctan\left(\frac{U_r}{U_x}\right)$ Results are shown in Figure 6(a), and Figure 6(b) respectively. For the magnitude results 95% of the data has an uncertainty of less than 10% and the average uncertainty for the entire domain is 3.66%. Similarly, when considering the uncertainty in flow direction, 92% of the data has an uncertainty of less than 50%, while 78.13% of the data has an uncertainty of less than 10%. As with Figure 5, both Figure 6(a) and (b) truncate the shown error at 15%.

After carefully reviewing the various GCI studies conducted, and the uncertainty due to mesh discretization, the most refined mesh was selected (N_1 = 454936 elements for $\psi_{enc} = 80$). The accuracy of this mesh was applied to all other enclosure sizes, which were designed based on the discussion found in Chapter 3.1.

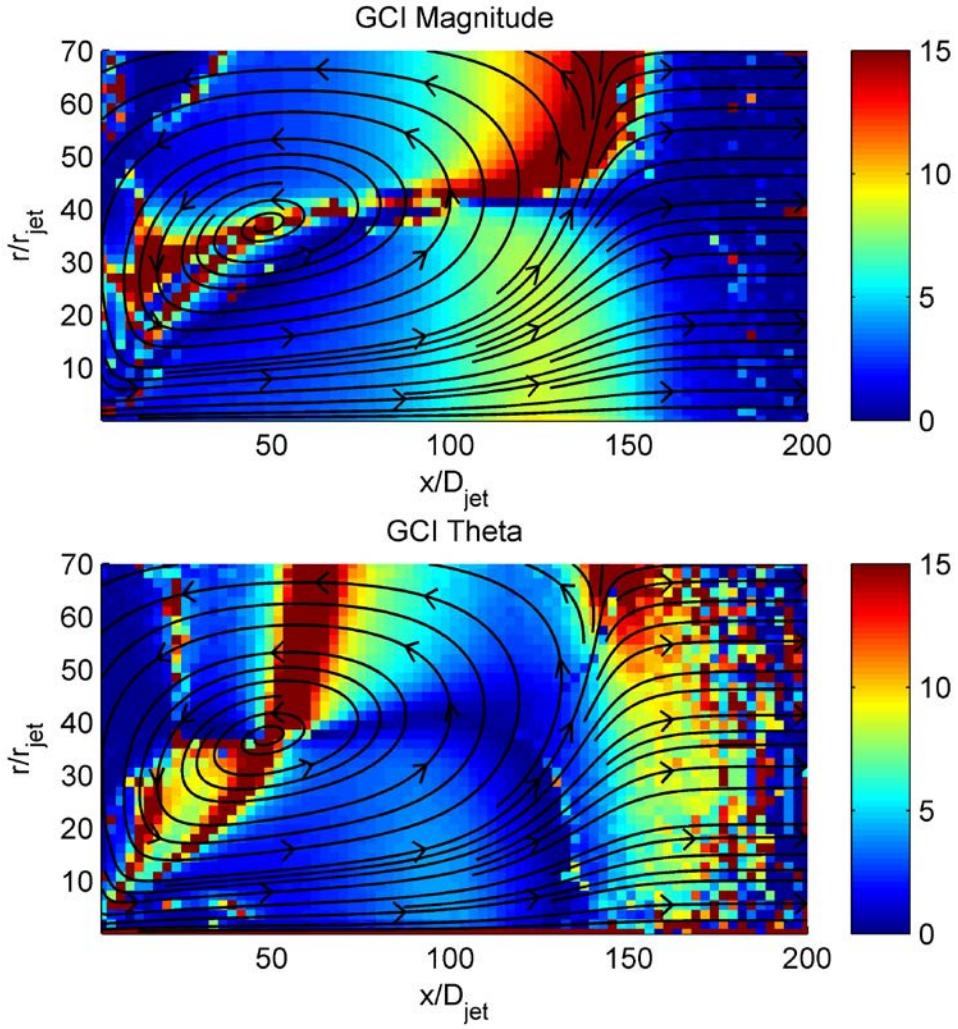

Figure 6 -(a) %GCI for |u| overlaid with flow Streamlines for $\psi_{enc} = 80$ and $\mathrm{Re}_{jet} = 32.2$

(b) %GCI for Θ overlaid with flow Streamlines for $\psi_{enc} = 80$ and $\mathrm{Re}_{jet} = 32.2$

4.0 FLOW REGIMES AND FLOW TRANSITIONS

4.1 CHARACTERIZATION OF FLOW REGIMES

For a fixed confinement size, $\psi_{enc} = 80$, the flow field was examined in order to determine important, useful characteristics. Shown in Figure 7 is the centerline velocity decay, $\frac{U_{jet}}{U_0}$, inlaid with radial profiles of the axial velocity, $\frac{U_x\left(\frac{r}{r_{jet}}\right)}{U_0}$. Similar results are shown for the jet half width, $\frac{r_{1/2}}{r_{jet}}$, in Figure 8. Regions of flow, similar to those described by Revuelta et al. [16] can be identified when analyzing Figure 7 and Figure 8 alongside of the streamlines of Figure 9. The first region, the free jet region, is the slender region, near the jet outlet, where the decay and spreading closely match those from a theoretical free jet. In this region, the centerline velocity decay and the half width growth are determined by Eqs. 2.1 and 2.2, respectively. These expressions suggest a linear dependence, for both centerline velocity decay and half width, with downstream distance (*x*), for a fixed ψ_{enc} and Re_{jet}. The axial location where the centerline decay deviates from the expected linear trend was identified when the difference between actual and predicted exceeded 10%. The inset of Figure 7 for $\frac{x}{D_{jet}} = 15$, shows the jet penetrating into

the domain with a profile similar to what one would expect from a free jet. There is little recirculation, revealed from the velocity magnitudes in the recirculation region.

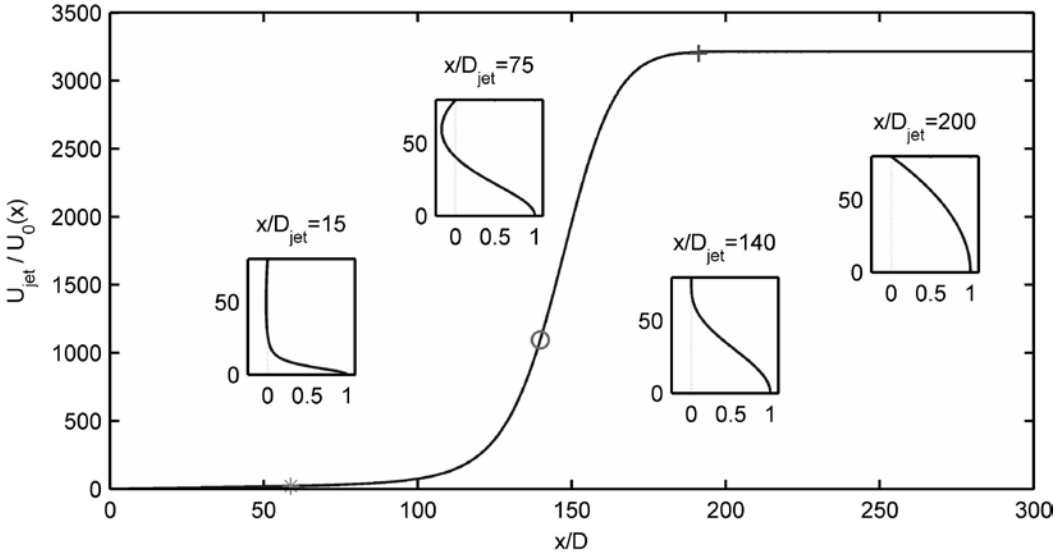

Figure 7- $\psi_{enc} = 80$, $\mathrm{Re}_{jet} = 32.2$. **Inlayed:** $\frac{U_x(r)}{U_{jet}}$ **vs** $\frac{r}{r_{jet}}$

$\frac{x_{lin}}{D_{jet}}$**: '*',** $\frac{x_{RL}}{D_{jet}}$**: 'o',** $\frac{x_{FD}}{D_{jet}}$**: '+'**

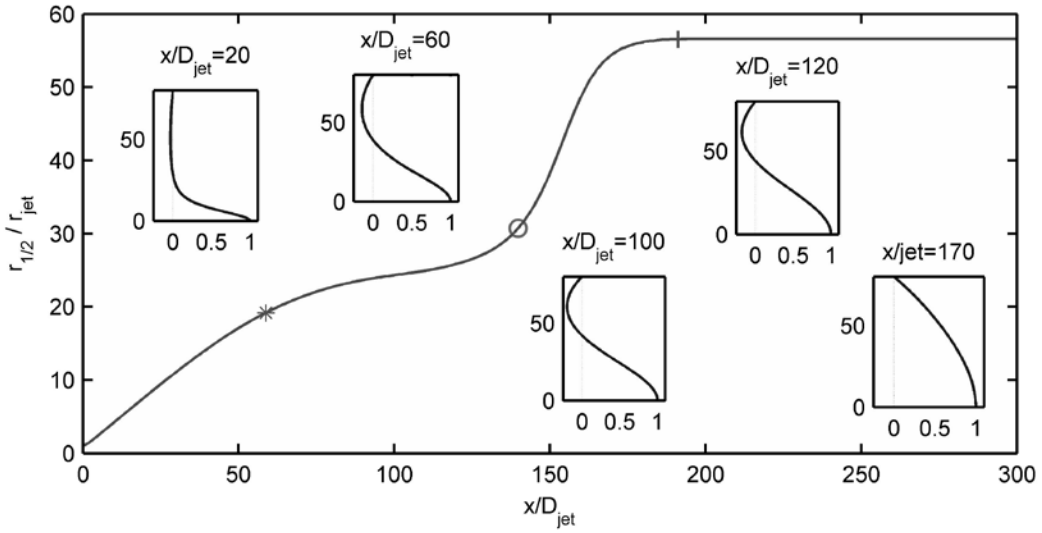

Figure 8 - $\psi_{enc} = 80$, $\mathrm{Re}_{jet} = 32.2$. **Inlayed:** $\frac{U_x(r)}{U_{jet}}$ **vs** $\frac{r}{r_{jet}}$

$\frac{x_{lin}}{D_{jet}}$**: '*',** $\frac{x_{RL}}{D_{jet}}$**: 'o',** $\frac{x_{FD}}{D_{jet}}$**: '+'**

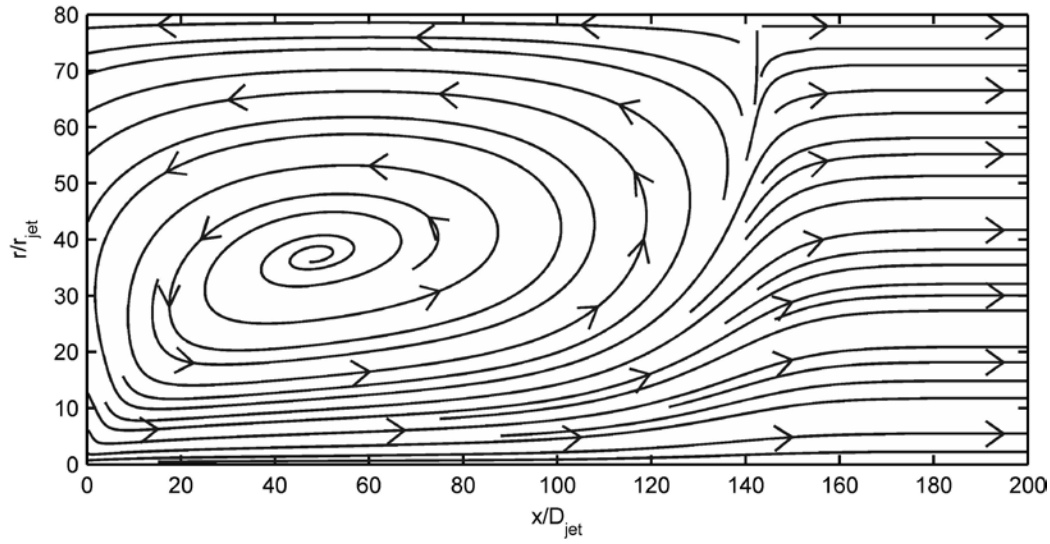

Figure 9 - Streamlines for $\psi_{enc} = 80$ **and** $\mathrm{Re}_{jet} = 32.2$

Beyond the free jet region, the jet begins to feel the effects of the large confinement. This region is referred to as the mixing region and for the data set analyzed in Figure 7 and Figure 8,

exists between $\frac{x}{D_{jet}} \approx 75$ (end of the free jet region) and $\frac{x_{RL}}{D_{jet}} \approx 140$ (axial location of the flow reattachment). Radial profiles of the flow at these two locations are shown as the second and third insets from Figure 7. Evident from the $\frac{x}{D_{jet}} = 60$ inset is the fact that the wall shear layer is developing in the opposite direction of the jet. The growth of the shear layer is present in both Figure 7, with the rapid velocity decay, and in Figure 8, where the growth rate of the half width begins to slow. The wall shear layer is the source of the recirculating eddy seen in Figure 9. At some distance downstream of the reattachment length, the flow becomes that of fully developed pipe flow (for the data in Figure 7, $\frac{x}{D_{jet}} = 200$). Therefore, the velocity profiles, and half width, at this location is that of a fully developed internal, pipe flow [33]. It is worth noting that the half width rapidly grows beyond the reattachment length before quickly plateauing as the flow becomes fully developed. The location of the transition to fully developed pipe flow was determined by analyzing the centerline velocity decay. The axial location where the centerline velocity became constant, within 0.2% was marked as the start of the fully developed flow region. It should be noted that the final value for centerline velocity can be predicted from the analytical expression for Poiseuille flow, Eq. 4.1 by making use of the fact that the maximum velocity occurs at the centerline ($r = 0$). The result can then be expressed in terms of the expected value for the centerline velocity decay, as shown in Eq. 4.2. As a note on convergence, the fully developed velocities were compared to theory, shown in Eq. 4.2, and found to have a maximum error of 0.55% and an average error of 0.32%. Since both the free jet region and the fully developed region have well know solutions, of specific interest in this thesis are the mixing and transition regions, and quantifying the demarcations between the various regions.

$$\frac{U(r)}{U_{jet}} = \frac{2}{\psi_{enc}^2}\left[1-\left(\frac{r}{r_{enc}}\right)^2\right] \tag{4.1}$$

$$\frac{U_{jet}}{U_0\left(x \geq x_{FD}\right)} = \frac{1}{2}\psi_{enc}^2 \tag{4.2}$$

4.2 DEPENDENCE ON ψ_{enc} AND Re_{jet}

The two metrics of most interest, namely the centerline velocity decay and the jet half width, are shown in Figure 10 and Figure 11 respectively, for various expansion ratios and $\mathrm{Re}_{jet} = 32.2$. Included on both plots are the locations where the centerline velocity deviates from linear free jet behavior $\left(x_{lin}\right)$, the location where the flow reattaches to the confinement wall, known as the reattachment length $\left(x_{RL}\right)$, and the location where the flow reaches fully developed, Poiseuille, behavior $\left(x_{FD}\right)$. The locations and trends of each of these transitions will be discussed in greater detail following, but as can be seen from these results, each simulation reveals an initial free jet behavior and ultimately transitions to internal Poiseuille flow.

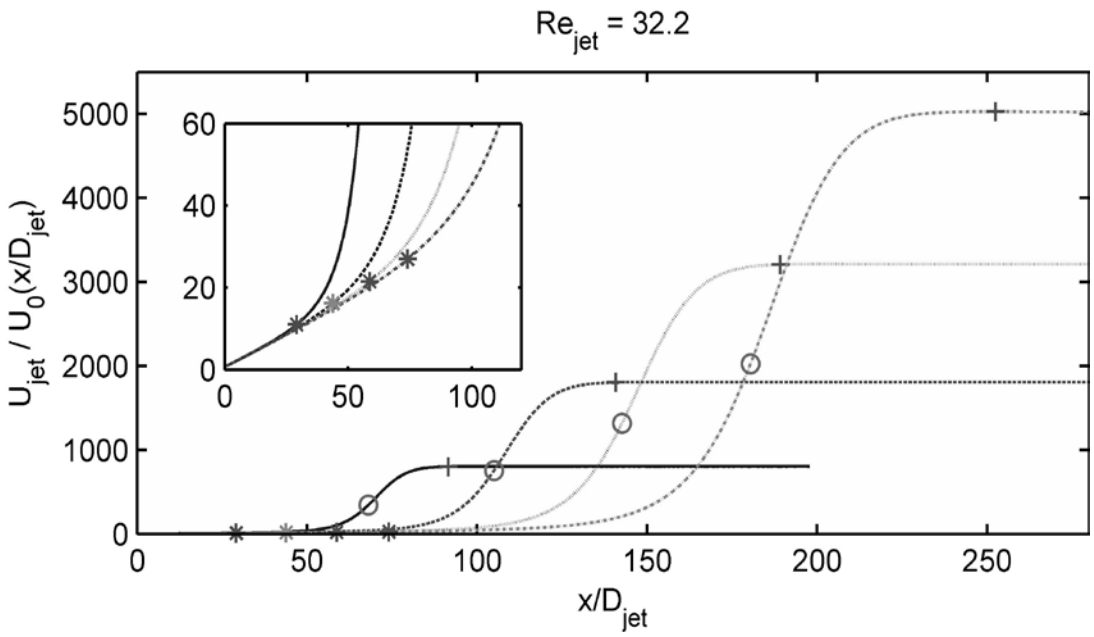

Figure 10 - $\frac{U_{jet}}{U_0(x)}$ **vs** $\frac{x}{D_{jet}}$ **for various** ψ_{enc}

$\psi_{enc} = 40$: '-', $\psi_{enc} = 60$: '--', $\psi_{enc} = 80$: '...', $\psi_{enc} = 100$: '-.-'

$\frac{x_{lin}}{D_{jet}}$: '*', $\frac{x_{RL}}{D_{jet}}$: 'o', $\frac{x_{FD}}{D_{jet}}$: '+'

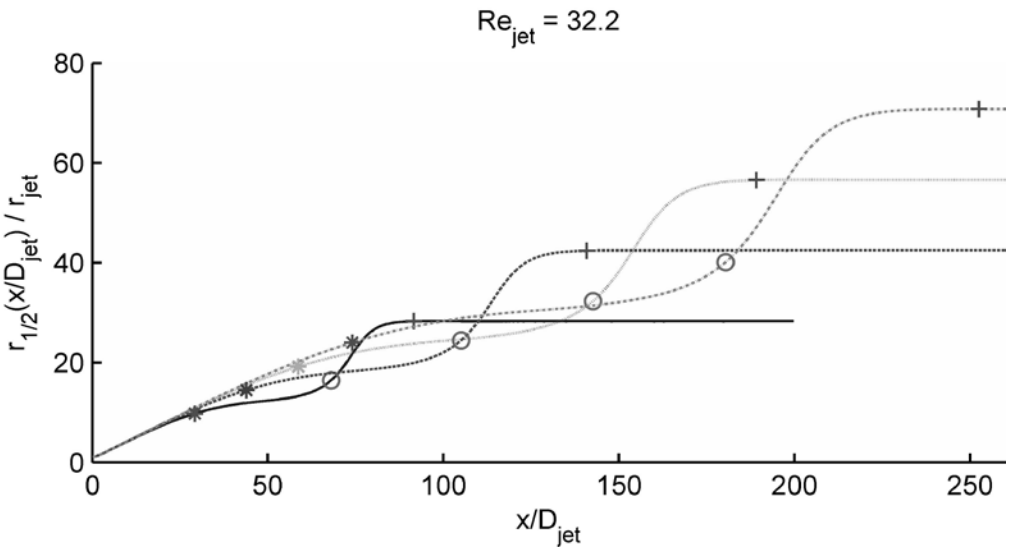

Figure 11 - $\frac{U_{jet}}{U_0(x)}$ **vs** $\frac{x}{D_{jet}}$ **for various** ψ_{enc}

$\psi_{enc} = 40$: '-', $\psi_{enc} = 60$: '--', $\psi_{enc} = 80$: '...', $\psi_{enc} = 100$: '-.-'

$\frac{x_{lin}}{D_{jet}}$: '*', $\frac{x_{RL}}{D_{jet}}$: 'o', $\frac{x_{FD}}{D_{jet}}$: '+

One of the goals of this study is to predict the behavior shown in these two figures. Figure 10 includes an inset linear region for small values of $\frac{x}{D_{jet}}$ to more clearly illustrate the deviation from Eqs. 2.1 and 2.2. Figure 12 (a), (b), and (c) illustrate the dependence for x_{lin}, x_{RL}, and x_{FD} respectively. For each of these figures, data is included for all three jet Reynolds numbers. As shown in Figure 12(a), x_{lin} varies linearly with ψ_{enc}. A least squares fit of the x_{lin} yields the expression in Eq. 4.3. The maximum absolute error was 1.3%, while the mean absolute error was 0.45%. Similar to what was done for x_{lin}, Eq. 4.4 fits the axial location of the reattachment point. This agrees well with Back and Roschke [19], who showed that x_{RL} approximately varies linearly as a function of Re_{jet}. An empirical fit of $\frac{x_{RL}}{D_{jet}}$ vs. ψ_{enc} is given in Eq. 4.4, which

yielded maximum and mean absolute errors of 4.14% and 1.43%, respectively. Data from Figure 12 (c) was fit as shown in Eq. 4.5. The maximum absolute error for this curve fit is 16.0%, while the mean error is only 4.19%.

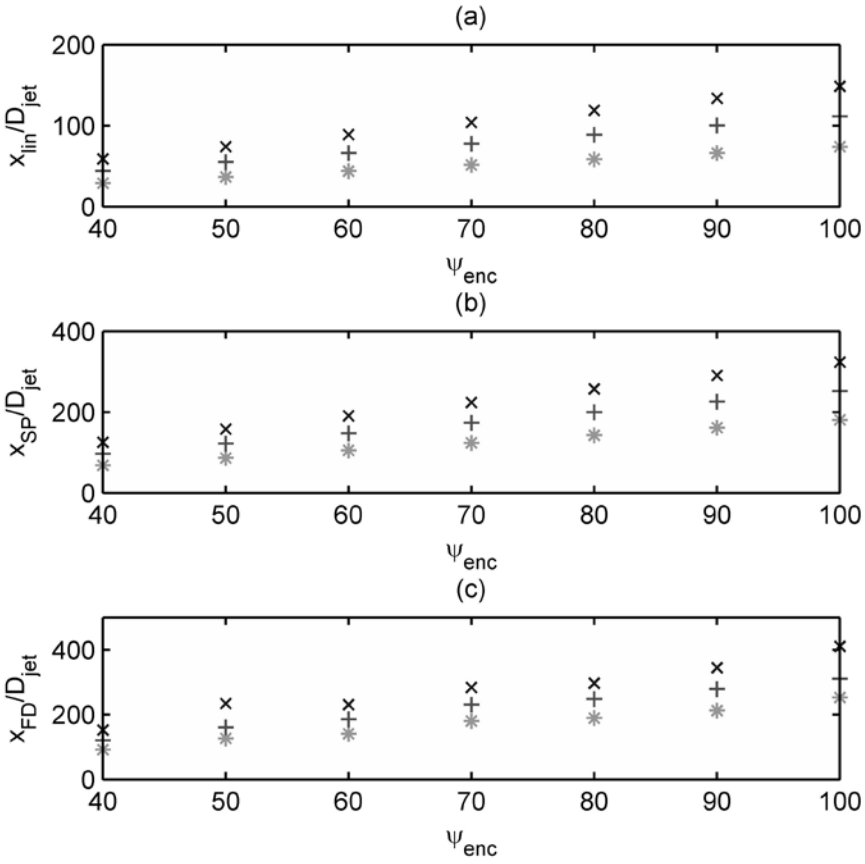

Figure 12 – (a) $\frac{x_{lin}}{D_{jet}}$, (b) $\frac{x_{RL}}{D_{jet}}$, (c) $\frac{x_{FD}}{D_{jet}}$ for various values of ψ_{enc} and Re_{jet}

$\mathrm{Re}_{jet} = 64.4$: **'x'**, $\mathrm{Re}_{jet} = 48.3$: **'+'**, $\mathrm{Re}_{jet} = 32.2$: **'*'**

$$\frac{x_{lin}}{D_{jet}} = 0.022\,\mathrm{Re}_{jet}^{1.014}\left(\psi_{enc}\right) \tag{4.3}$$

$$\frac{x_{RL}}{D_{jet}} = 0.091\mathrm{Re}_{jet}^{0.856}\left(\psi_{enc}\right) \tag{4.4}$$

$$\frac{x_{lin}}{D_{jet}} = 0.022\,\mathrm{Re}_{jet}^{1.014}\left(\psi_{enc}\right) \tag{4.5}$$

5.0 CENTERLINE VELOCITY AND HALF WIDTH

Of particular importance in the current work was to develop an expression for the jet centerline velocity and half width valid for $\frac{x}{D_{jet}} \le \frac{1}{2}\frac{x_{RL}}{D_{jet}}$. For the centerline velocity, the linear free jet behavior, Eq. 2.1, was subtracted from the obtained profiles. The result was found to be described well with an exponential decay according to:

$$\frac{U_{jet}}{U_0\left(x/D_{jet}\right)} - \left(m\frac{x}{D_{jet}} + b\right) = A\left(\mathrm{Re}_{jet}, \psi_{enc}\right)\left(e^{B\left(\mathrm{Re}_{jet},\psi_{enc}\right)\frac{x}{D_{jet}}} - 1\right) \qquad 5.1$$

Note that the linear jet decay parameters, (*m* and *b*) are found by fitting the data from the largest enclosure, $\psi_{enc} = 100$, in the region $10 \le \frac{x}{D_{jet}} \le 30$. The two values found from a least squares curve fit are used when analyzing all other enclosure sizes. The next task was to determine appropriate expressions for *A* and *B* as they relate to Re_{jet} and expansion ratio ψ_{enc}. This data, out to 50% of the reattachment length is shown in Fig. 11, which suggests that both *A* and *B* are dependent on expansion ratio, while only *B* is sensitive to Re_{jet}. An exponential dependence on ψ_{enc} combined with a power law relationship in Re_{jet} is proposed to fully describe the behavior seen for *A* and *B*. Additionally, it is noted that as the expansion becomes very large, the fit parameter *B* approaches zero. Evaluating Eqs. 5.1 with $B = 0$ reveals a centerline behavior completely described by the linear, free jet expressions. This is expected

since the infinitely large enclosure would have no impact on the jet. The expressions for $A(\mathrm{Re}_{enc},\psi_{enc})$ and $B(\mathrm{Re}_{enc},\psi_{enc})$ are provided below.

$$A(\mathrm{Re}_{jet},\psi_{enc}) = 4.83\cdot 10^{-4}\,\mathrm{Re}_{jet}^{-0.202}\,\psi_{enc} \qquad 5.2$$

$$B(\mathrm{Re}_{jet},\psi_{enc}) = 7.466\,\mathrm{Re}_{jet}^{-0.931}\,e^{-0.016\psi_{enc}} \qquad 5.3$$

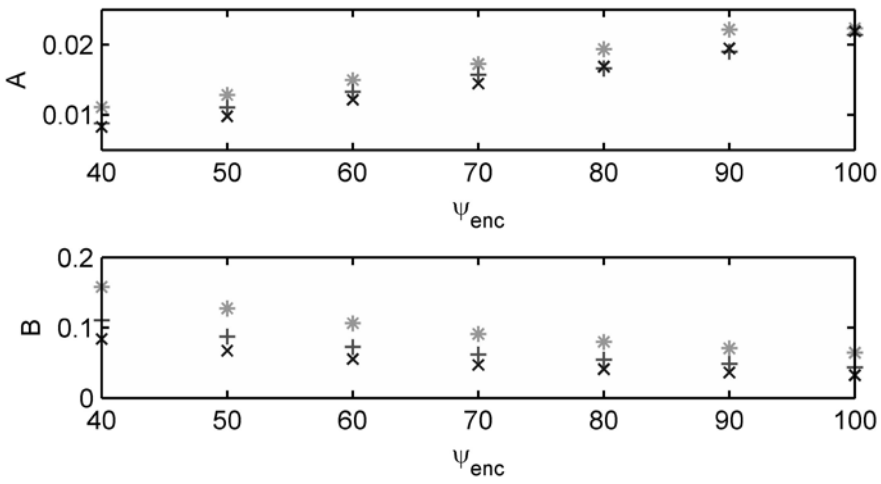

Figure 13 - Fit parameters: (a) $A(\mathrm{Re}_{jet},\psi_{enc})$ and (b) $B(\mathrm{Re}_{jet},\psi_{enc})$ in Eq. 5.1

$\mathrm{Re}_{jet} = 64.4$: **'x'**, $\mathrm{Re}_{jet} = 48.3$: **'+'**, $\mathrm{Re}_{jet} = 32.2$: **'*'**

In order to verify the accuracy of Eqs. 5.2 and 5.3, the maximum absolute error and the mean absolute error were calculated. The absolute error was defined according to Eq. 5.4. The maximum absolute error was 7.59% and the mean absolute error was 3.45%. Shown in Figure 14 is simulation data for the jet centerline velocity and the centerline velocity as predicted by the inverse of the correlation 5.1 for a fixed expansion ratio, $\psi_{enc} = 80$ and all three jet Reynolds numbers (32.2, 48.3, 64.4). For each Reynolds number and enclosure size simulated, the error in the curve fit is small near the jet inlet but begins growing as the jet feels the effect of confinement and transitions away from free jet behavior. The maximum absolute error in each case occurred far from the inlet at the furthest downstream location fitted.

$$error = \left| \frac{\frac{U_{jet}}{U_0(x)} - \left(m\frac{x}{D_{jet}} + b \right) - A\left(\mathrm{Re}_{jet}, \psi_{enc}\right)\left(e^{B\left(\mathrm{Re}_{jet}, \psi_{enc}\right)\frac{x}{D_{jet}}} - 1 \right)}{\frac{U_{jet}}{U_0(x)}} \right| \qquad 5.4$$

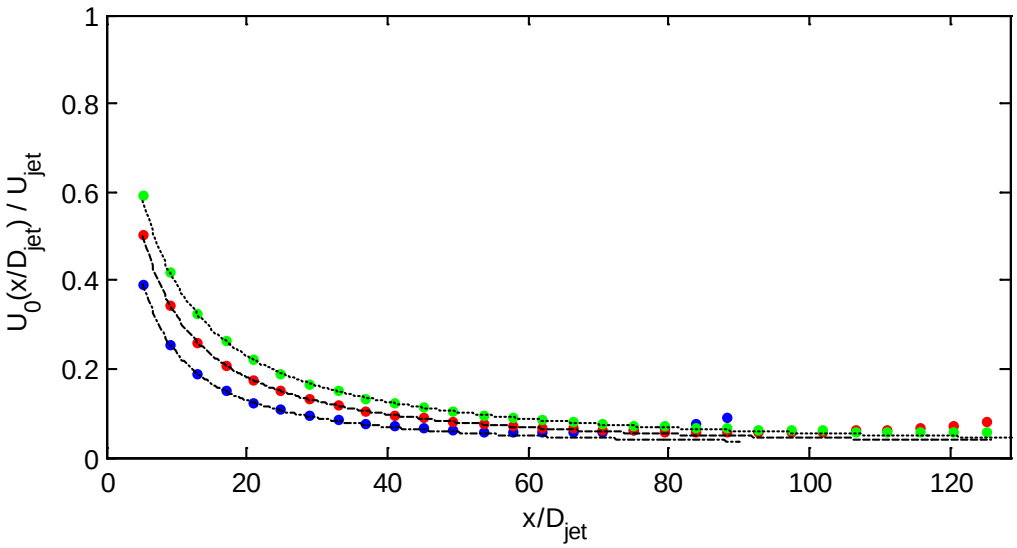

Figure 14 - Plot of simulation values (black) and correlation values

($\mathrm{Re}_{jet} = 64.4$ **: 'x',** $\mathrm{Re}_{jet} = 48.3$ **: 'x',** $\mathrm{Re}_{jet} = 32.2$ **: 'x')**

$\mathrm{Re}_{jet} = 64.4$ **: '...',** $\mathrm{Re}_{jet} = 48.3$ **: '--',** $\mathrm{Re}_{jet} = 32.2$ **: '-.-**

In addition to being able to predict the centerline velocity, similar efforts were made to establish correlations for the behavior of the half width for the same range of x $\left(\frac{x}{D_{jet}} \le \frac{1}{2}\frac{x_{RL}}{D_{jet}} \right)$. As before, the expected free jet behavior, extracted from the case with expansion ratio $\psi_{enc} = 100$, was subtracted from the half width simulation data. This difference was fit according to the power law relationship shown in Eq. 5.5. Similar to the approach with centerline fits, the two coefficients (*C* and *D*) are dependent on Re_{jet} and ψ_{enc}. Shown in Figure 15 is a plot of these parameters to illustrate the Re_{jet} and ψ_{enc} dependence. Additional power law correlations

for C and D are given in Eqs. 5.6 and 5.6 respectively. As before, it is noted that as ψ_{enc} approaches infinity, C goes to zero, which implies for large expansion ratios, the curve fit mimics free jet behavior. Using the assigned curve fits, the mean absolute error in the half width fit is 28.63%, while the maximum absolute error is 65.3%.

$$\frac{r_{1/2}}{r_{jet}} - \left(m_{HW} \frac{x}{D_{jet}} + b_{HW} \right) = C\left(\mathrm{Re}_{jet}, \psi_{enc}\right) \left(\frac{x}{D_{jet}} \right)^{D(\psi_{enc})} \quad 5.5$$

$$C\left(\mathrm{Re}_{jet}, \psi_{enc}\right) = -4.1 \cdot 10^{5}\, \mathrm{Re}_{jet}^{-3.6}\, \psi_{enc}^{-3.2} \quad 5.6$$

$$D\left(\psi_{enc}\right) = 2.4517 \psi_{enc}^{0.1} \quad 5.7$$

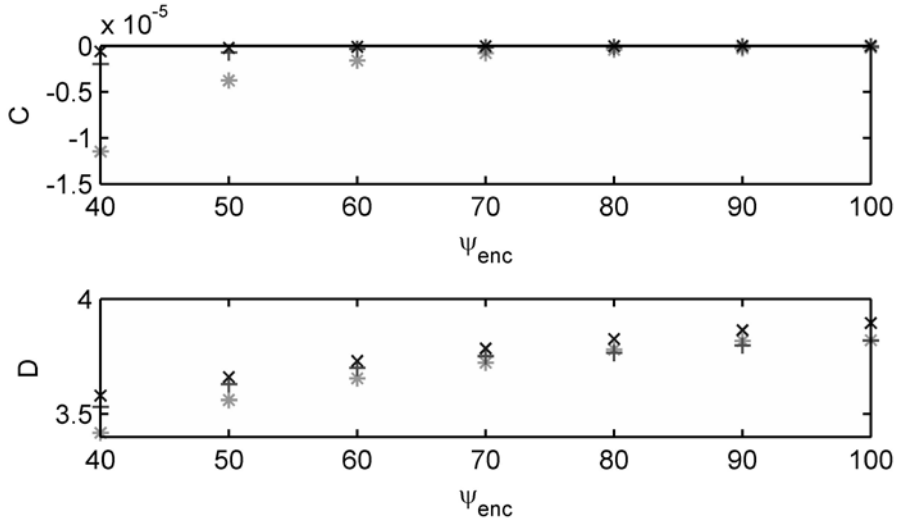

Figure 15 - $C\left(\mathrm{Re}_{jet}, \psi_{enc}\right)$ **and (b)** $D\left(\psi_{enc}\right)$ **in Eq. 5.5**

$\mathrm{Re}_{jet} = 64.4$**: 'x',** $\mathrm{Re}_{jet} = 48.3$**: '+',** $\mathrm{Re}_{jet} = 32.2$**: '*'**

6.0 CONCLUSIONS

In the present study, confined, laminar round jets were studied as the jet Reynolds number, Re_{jet} and the expansion ratio, $\psi_{enc} = \frac{r_{enc}}{r_{jet}}$, were varied. Presently three Reynolds numbers, 32.2, 48.3, and 64.4 have been examined. Additionally, seven expansion ratios varying from 40-100 were investigated. Several points of interest were identified in the flow, including the location where the jet begins to deviate from linear behavior, the reattachment length, and the location where the flow begins to behave as internal, Poiseuille pipe flow. $\frac{U_{jet}}{U_o(x)}$ and $\frac{r_{1/2}}{r_{jet}}$ were investigated to determine qualitative flow regions, namely the free jet region, mixing region, transitional region, and the fully developed region, demarcated by the previously mentioned points of interest. Additional effort was taken to understand how each point of interest behaved as a function of Re_{jet} and ψ_{enc}. Correlations were developed for $\frac{x_{lin}}{D_{jet}}$, $\frac{x_{RL}}{D_{jet}}$, and $\frac{x_{FD}}{D_{jet}}$. Finally, correlations were developed for $\frac{U_{jet}}{U_o(x)}$ and $\frac{r_{1/2}}{r_{jet}}$ out to 50% of $\frac{x_{RL}}{D_{jet}}$.

Of additional interest is to conduct a similar study for plane jets, whose decay and spread rates vary differently from those of a round jet, but apply to different families of applications. The current study also sets the stage for similar quantitative analysis of the enclosure effects on a turbulent jet, a scenario of great importance in numerous applications. Beyond turbulent

confined jets, complex issues involving thermally fluctuating flows, and the heat transfer to confinement is of interest. Ongoing work will investigate impinging jets, both numerically with RANS and LES, and experimentally using PIV and hot-wire anemometry. Moreover, additional work should look into the design and scaling of experiments and numerical models for better understanding the flow in next generation reactors.

APPENDIX A

SETUP AND EXECUTION OF OPENFOAM ® CFD STUDY

A.1 PRELIMINARY STUDIES

In order to develop a detailed, systematic approach for studying confined laminar round jets, initial studies were conducted for all three Reynolds numbers and expansion ratios ranging from 40-220. For the preliminary studies, the mesh described in Chapter 3.1 was used, but with very few elements in the radial direction, and very large gradings. In particular, the mesh studied had two elements per jet radius in the shear layer, and a grading of 10 in the expansion and a grading of $1/10^{th}$ in the contraction. Utilizing this coarse mesh, several immediate trends were noticed in the simulation behavior.

First, while most trends shown in Figure 16 are the same as presented previously, one immediate difference is the over shoot present near the reattachment length for large enclosure sizes. Investigation of the location of maximum centerline velocity found that with increased iterations, this location moved back and forth in the domain, while the magnitude of the maximum velocity continued to decrease towards the expected fully developed value. Moreover, after investigation the iterative behavior of several points in the domain, including the location of maximum velocity, the location of the stagnation point, the deviation from linear free-jet

behavior, and the onset of fully developed flow, it was found the location of maximum velocity was always slowest to converge, and one of the most important points to monitor.

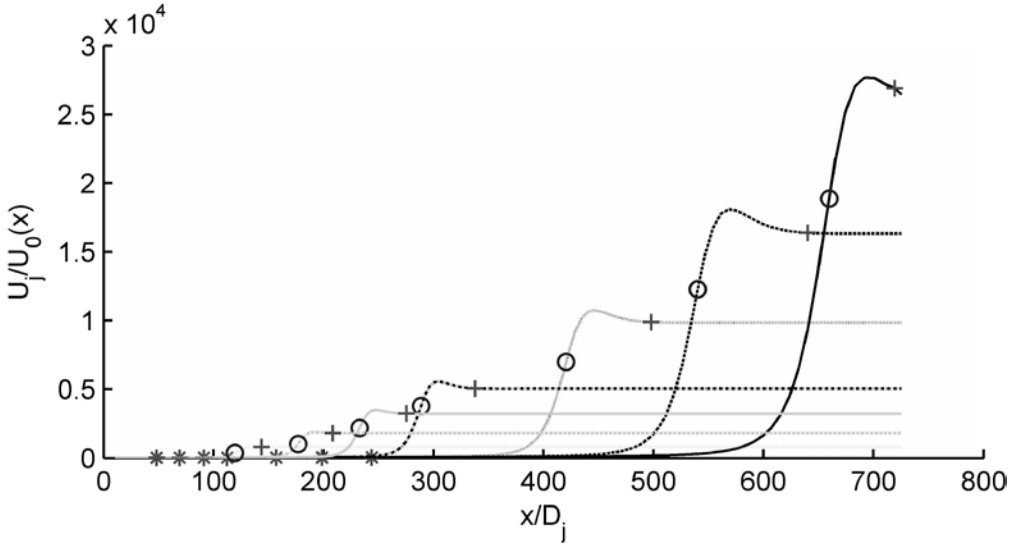

Figure 16 - $\frac{U_{jet}}{U_0(x)}$ **vs** $\frac{x}{D_{jet}}$ **for various** ψ_{enc}

$\psi_{enc} = 40$: '...', $\psi_{enc} = 60$: '--', $\psi_{enc} = 80$: '-', $\psi_{enc} = 100$:

'-.-', $\psi_{enc} = 140$: '...', $\psi_{enc} = 180$: '--', $\psi_{enc} = 220$: '--'

$\frac{x_{lin}}{D_{jet}}$: '*', $\frac{x_{RL}}{D_{jet}}$: 'o', $\frac{x_{FD}}{D_{jet}}$: '+'

Additionally, several observations on the nature of convergence were made. The length required for the flow to become fully developed increases as a function of enclosure size, thus, cases with small expansion ratios do not require large downstream lengths. This was later confirmed as shown in Eq. 4.5. Additionally, attempts at obtaining converged solutions for large enclosures, $\psi_{enc} >> 100$ was found to be computationally cost prohibitive.

Finally, consideration was given to the effect of upstream length on flow behavior. In order to best determine these effects, several different tests were ran. First, a case with the

upstream length in the experimental study of Hussein (1994) was used [27], with $\mathrm{Re}_{jet} = 32.2$ and $\psi_{enc} = 180$. Note that due to the large confinement size, iterative convergence was never achieved near the reattachment length. It was observed that the primary recirculating eddy, shown in Figure 9, penetrated some distance upstream of the jet inlet. Further upstream of this point was a cascade of smaller eddies of decreasing vorticity until the velocity became zero at the upstream wall. The vortex cascade is shown in Figure 17.

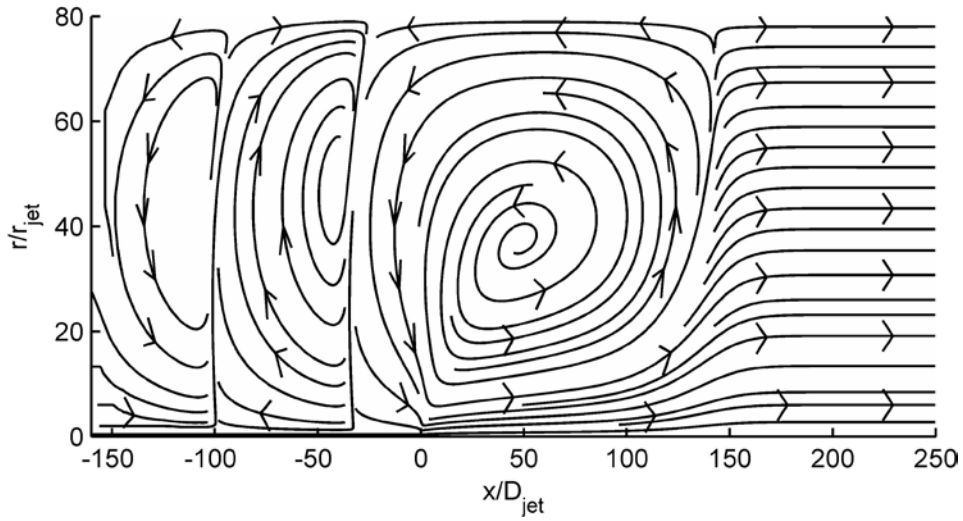

Figure 17 - Streamlines for $\mathrm{Re}_{jet} = 32.2$ and $\psi_{enc} = 80$ with upstream eddies shown

After establishing the distance upstream that the main recirculating eddy reaches upstream of the jet inlet, two subsequent studies were conducted. First, a study was run which placed the upstream wall a distance closer to the jet than the eddy had reached. Second, a study was run which placed the upstream wall closer to the jet, but still further upstream than the eddy had reached. When placing the wall too close to the jet inlet, the size of the primary recirculating eddy was diminished. However, when the wall was sufficiently far upstream, the size of the primary recirculating eddy, as determined by the reattachment length and the location of the center of the eddy, did not feel the effects of the subsequent upstream eddies. This behavior is

perhaps due to the large vorticity of the primary eddy when compared with subsequent eddies in the upstream direction.

A.2 MESH GENERATION

In OpenFOAM ®, generation of the mesh detailed in Chapter 3.1, and shown in Figure 4, is accomplished utilizing the “blockMesh” utility. The blockMesh utility utilizes a dictionary file, “blockMeshDict,” provided in Chapter A.2.1. This includes a case utilizing 8 elements in the radial direction of the jet, and 517 downstream elements with a 10 m downstream length. The blockMeshDict shown utilizes predefined variables for defining vertices locations, the number of elements in each layer, and the grading in layers where non-uniform mesh size was desired. In order to generate the blockMeshDict associated with the studied geometry, a MATLAB script was written which automated calculation of pertinent mesh constraints. The script is provided in Chapter A.2.2.

For the mesh generation script in Chapter A.2.2, ten user inputs are specified and used to calculate all other relevant parameters. The user inputs relating to geometry are jet radius, enclosure radius, upstream length, and downstream length. The parameters related to mesh design are wedge angle, shear layer radius, mixing layer radius, and the number of elements within the jet radius, as well as the number of elements downstream of the jet in the axial direction. For regions with variable cell size, or grading, the size of the first element was selected to match the size of the last element of the boarding region. OpenFOAM ® requires the ratio between the first cell and last cell in the block to be specified, thus, in order to calculate this, a 5% increase between subsequent cells, referred to as the ratio δ, was selected. Utilizing

this criterion, it is possible to write the length of the block as a geometric series, based on a first cell with known size. This is shown in Eq. 5.8, where *a* is the size of the first cell, and *N* is the number of cells. Since the length of the region, or block, and the ratio are previously determined, the number of cells can now be calculated. Note that since an integer number of cells is necessary, the actual ratio is not exactly 5%, but as close as possible while still maintaining the discrete requirements of the total number of cells. In order to standardize the procedure, the number of cells was always rounded up, hence insuring the ratio was less than 5%. The ratio was then recalculated using Eq. 5.8, except this time *L* and *N* were known. The new ratio was then used to calculate the grading, or rate between the last cell size and the first cell size as δ^{N-1}.

$$L = a\sum_{i=0}^{N-1}\delta^{i} \simeq \frac{1-\delta^{N}}{1-\delta} \tag{5.8}$$

A.2.1 blockMeshDict

```
  /*--------------------------------*- C++ -*----------------------------------*\
| =========                 |                                                 |
| \\      /  F ield         | OpenFOAM: The Open Source CFD Toolbox           |
|  \\    /   O peration     | Version:  1.7.1                                 |
|   \\  /    A nd           | Web:      www.OpenFOAM.com                      |
|    \\/     M anipulation  |                                                 |
\*---------------------------------------------------------------------------*/
FoamFile
{
    version     2.0;
    format      ascii;
    class       dictionary;
    object      blockMeshDict;
}
// * * * * * * * * * * * * * * * * * * * * * * * * * * * * * * * * * * * * * //

convertToMeters 1;
```

```
// This code constructs a circular domain, instead of Hussein's square domain.  I
am still using an inlet pipe like he does.  This is easily omitted if we care to
do so.

//- This section of code defines the properties for jet
jetRadius     0.010000;
jetPosWidth   0.000175;
jetNegWidth   -0.000175;
jetElements       8;
jetGrading    1.000000;

//- This section of code defines the properties for shearLayer
shearLayerRadius    0.200000;
shearLayerPosWidth  0.003491;
shearLayerNegWidth  -0.003491;
shearLayerElements     152;
shearLayerGrading   1.000000;

//- This section of code defines the properties for innerLayer
innerLayerRadius    0.555000;
innerLayerPosWidth  0.009688;
innerLayerNegWidth  -0.009688;
innerLayerElements      55;
innerLayerGrading   14.762709;

//- This section of code defines the properties for wallLayer
wallLayerRadius     0.900000;
wallLayerPosWidth   0.015710;
wallLayerNegWidth   -0.015710;
wallLayerElements       55;
wallLayerGrading    14.762709;

//- This section of code defines the properties for enclosure
enclosureRadius     1.000000;
enclosurePosWidth   0.017455;
enclosureNegWidth   -0.017455;
enclosureElements       80;
enclosureGrading    1.000000;

//- This section of code defines the properties for downstream
downstreamLength    10.000000;
downstreamElements          1367;
downstreamGrading   2.000000;

//- This section of code defines the properties for upstream
upstreamLength      -4.000000;
upstreamElements       547;
upstreamGrading     2.000000;



//-----------------------------------------------------------------------
```

```
vertices
(
    // These define the inner fluid layer and jet
      (0  0  0)
    //- Jet
      (0    $jetRadius         $jetPosWidth)
      (0    $jetRadius         $jetNegWidth)
    //-shear layer Layer
      (0    $shearLayerRadius        $shearLayerPosWidth)
      (0    $shearLayerRadius        $shearLayerNegWidth)
    //-inner layer Layer
      (0    $innerLayerRadius        $innerLayerPosWidth)
      (0    $innerLayerRadius        $innerLayerNegWidth)
    //-outer Layer (up to wall shear layer)
      (0    $wallLayerRadius         $wallLayerPosWidth)
      (0    $wallLayerRadius         $wallLayerNegWidth)
    // These points define the outer layer on the front
      (0    $enclosureRadius   $enclosurePosWidth)
      (0    $enclosureRadius   $enclosureNegWidth)

    //- Downstream Length
      ($downstreamLength  0  0)
    //- Jet
      ($downstreamLength $jetRadius         $jetPosWidth)
      ($downstreamLength $jetRadius         $jetNegWidth)
    //-shear layer Layer
      ($downstreamLength $shearLayerRadius        $shearLayerPosWidth)
      ($downstreamLength $shearLayerRadius        $shearLayerNegWidth)
    //-inner layer Layer
      ($downstreamLength $innerLayerRadius        $innerLayerPosWidth)
      ($downstreamLength $innerLayerRadius        $innerLayerNegWidth)
    //-outer Layer (up to wall shear layer)
      ($downstreamLength $wallLayerRadius         $wallLayerPosWidth)
      ($downstreamLength $wallLayerRadius         $wallLayerNegWidth)
    // These points define the outer layer on the front
      ($downstreamLength $enclosureRadius   $enclosurePosWidth)
      ($downstreamLength $enclosureRadius   $enclosureNegWidth)

    // upstream face
    //- Jet
      ($upstreamLength   $jetRadius         $jetPosWidth)
      ($upstreamLength   $jetRadius         $jetNegWidth)
    //-shear layer Layer
      ($upstreamLength   $shearLayerRadius        $shearLayerPosWidth)
      ($upstreamLength   $shearLayerRadius        $shearLayerNegWidth)
    //-inner layer Layer
      ($upstreamLength   $innerLayerRadius        $innerLayerPosWidth)
      ($upstreamLength   $innerLayerRadius        $innerLayerNegWidth)
    //-outer Layer (up to wall shear layer)
      ($upstreamLength   $wallLayerRadius         $wallLayerPosWidth)
      ($upstreamLength   $wallLayerRadius         $wallLayerNegWidth)
```

```
    // These points define the outer layer on the front
      ($upstreamLength   $enclosureRadius   $enclosurePosWidth)
      ($upstreamLength   $enclosureRadius   $enclosureNegWidth)
);

blocks
(
    //- These hex's define the jet
    hex (0 11 13 2 0 11 12 1) ($downstreamElements $jetElements 1) simpleGrading
($downstreamGrading $jetGrading 1)
    //- Jet shear layer
    hex (2 13 15 4 1 12 14 3) ($downstreamElements $shearLayerElements 1)
simpleGrading ($downstreamGrading  $shearLayerGrading 1)
    //- inner jet mixing layer
    hex (4 15 17 6 3 14 16 5) ($downstreamElements $innerLayerElements  1)
simpleGrading ($downstreamGrading $innerLayerGrading 1)
    //- outer jet mixing layer (definied with opposite y)
    hex (7 18 16 5 8 19 17 6) ($downstreamElements $wallLayerElements  1)
simpleGrading ($downstreamGrading $wallLayerGrading 1)
    //- wall shear layer
    hex (8 19 21 10 7 18 20 9) ($downstreamElements $enclosureElements  1)
simpleGrading ($downstreamGrading $enclosureGrading 1)

    //-Upstream section
    //- Jet shear layer
    hex (1 22 24 3 2 23 25 4) ($upstreamElements $shearLayerElements 1)
simpleGrading ($upstreamGrading  $shearLayerGrading 1)
    //- inner jet mixing layer
    hex (3 24 26 5 4 25 27 6) ($upstreamElements $innerLayerElements  1)
simpleGrading ($upstreamGrading $innerLayerGrading 1)
    //- outer jet mixing layer (definied with opposite y)
    hex (8 29 27 6 7 28 26 5) ($upstreamElements $wallLayerElements  1)
simpleGrading ($upstreamGrading $wallLayerGrading 1)
    //- wall shear layer
    hex (7 28 30 9 8 29 31 10) ($upstreamElements $enclosureElements  1)
simpleGrading ($upstreamGrading $enclosureGrading 1)
);

edges
(
);

boundary
(
    inlet
    {
      type patch;
      faces
        (
        (0 0 1 2)
      );
    }
```

```
outlet
{
  type patch;
  faces
  (
        //Back Wall..
        (11 11 12 13)
        (12 14 15 13)
        (14 16 17 15)
        (16 18 19 17)
        (18 20 21 19)
  );
}

allWalls
{
  type wall;
  faces
  (
    //- Side Walls
    (9 20 21 10)
    (9 10 31 30)

    //- Upstream Wall
    (22 23 25 24)
    (24 25 27 26)
    (26 27 29 28)
    (28 29 31 30)

    //-Pipe walls..
    (1 2 23 22)
  );
}

front
{
  type wedge;
  faces
  (
  (0 1 12 11)
  (1 3 14 12)
  (3 5 16 14)
  (5 7 18 16)
  (7 9 20 18)
  (1 3 24 22)
  (3 5 26 24)
  (5 7 28 26)
  (7 9 30 28)
  );
}
```

```
    back
    {
      type wedge;
      faces
      (
      (0 2 13 11)
      (2 4 15 13)
      (4 6 17 15)
      (6 8 19 17)
      (8 10 21 19)
      (2 4 25 23)
      (4 6 27 25)
      (6 8 29 27)
      (8 10 31 29)
      );
    }

    planeAxis
    {
      type symmetryPlane;
      faces
      (
            (0 11 11 0)
      );
   }
);

mergePatchPairs
(
);

// ************************************************************************* //
```

A.2.2 Meshing Script

```
%+++++++++++++++USER INPUTS++++++++++++++++++++++
r_j=.01;       %Jet radius r_{jet} [meters]
angle=1*pi/180; %Wedge Angle[radians]
upstream=-4; % upstream wall coordinate  [meters]

radial_elements=20; % Elements in jet radius

R=0.8; %\eta_{enc}*r_{jet}  Enclosure radius [meters]
axial_elements=1200; %Number of elements downstream of jet
downstream=6; %Downstream outlet length [meters]
```

```
shearLayer=20*r_j;  %Width of the shear layer [meters]
wallLayer=R-1/2*shearLayer;  %radial coordinate for wall layer
innerLayer=(R-r_j-(R-wallLayer)-shearLayer)/2+r_j+shearLayer;  %radial
coordinate for mixing layer

%+++++++++++++END OF USER INPUTS++++++++++++++++++++
%++++++++++++++++++++++++++++++++++++++++++++++++++

%# of elements in jet radius
elementSize=r_j/radial_elements;

%These are evaluation options for some root finding
options = optimset('MaxFunEvals' ,1000, 'Display', 'on','TolFun',10^(-6));

dimensions(1).name='jet';
dimensions(2).name='shearLayer';
dimensions(3).name='innerLayer';
dimensions(4).name='wallLayer';
dimensions(5).name='enclosure';
dimensions(6).name='downstream';
dimensions(7).name='upstream';

dimensions(1).radius=r_j;
dimensions(2).radius=shearLayer;
dimensions(3).radius=innerLayer;
dimensions(4).radius=wallLayer;
dimensions(5).radius=R;
dimensions(6).radius=downstream;
dimensions(7).radius=upstream;

dimensions(1).grading=1;
dimensions(2).grading=1;

delta=1.05;
n=ceil(log((innerLayer-shearLayer)*(delta-1)/elementSize)/log(delta));
delta=fsolve(@(x) (x^n-(innerLayer-shearLayer)/elementSize*(x-1)-
1),1.1,options);

dimensions(3).grading=delta^(n-1);
dimensions(4).grading=dimensions(3).grading;
dimensions(5).grading=1;
dimensions(6).grading=2;
dimensions(7).grading=2;

dimensions(1).elements=r_j/elementSize;
dimensions(2).elements=(dimensions(2).radius-
dimensions(1).radius)*dimensions(1).elements/dimensions(1).radius;
dimensions(3).elements=n;
dimensions(4).elements=n;
dimensions(5).elements=(dimensions(5).radius-
dimensions(4).radius)*dimensions(1).elements/dimensions(1).radius;
dimensions(6).elements=axial_elements;
dimensions(7).elements=round(abs(upstream/downstream)*dimensions(6).elements)
;
```

```
for i=1:5
    dimensions(i).posWidth=tan(angle)*dimensions(i).radius;
    dimensions(i).negWidth=-1*tan(angle)*dimensions(i).radius;
end

file = fopen(['R0' num2str(dimensions(1).elements) '_A8000('
num2str(dimensions(6).elements) ' X ' num2str(downstream) ')_' num2str(R/r_j)
'.txt'],'w');

for i=1:5
    fprintf(file,'//- This section of code defines the properties for %s\n',
dimensions(i).name);
    fprintf(file,'%sRadius\t %f;\n', dimensions(i).name,
dimensions(i).radius);
    fprintf(file,'%sPosWidth\t %f;\n', dimensions(i).name,
dimensions(i).posWidth);
    fprintf(file,'%sNegWidth\t %f;\n', dimensions(i).name,
dimensions(i).negWidth);
    fprintf(file,'%sElements\t %6.0f;\n', dimensions(i).name,
dimensions(i).elements);
    fprintf(file,'%sGrading\t %f;\n\n', dimensions(i).name,
dimensions(i).grading);
end

for i=6:7
    fprintf(file,'//- This section of code defines the properties for %s\n',
dimensions(i).name);
    fprintf(file,'%sLength \t %f;\n', dimensions(i).name,
dimensions(i).radius);
    fprintf(file,'%sElements \t %6.0f;\n', dimensions(i).name,
dimensions(i).elements);
    fprintf(file,'%sGrading \t %f;\n\n', dimensions(i).name,
dimensions(i).grading);
end

fclose(file);
```

A.3 NUMERICAL DISCRETIZATION SCHEMES AND CONVERGENCE CONTROL

All numerical discretization was done using linear methods when available. A list of available discretization is available in the OpenFOAM® user guide. An example of the fvSchemes dictionary, used for setting the desired discretization is shown in Chapter A.2.1. Additionally, an

example of the residual control used for the simulations, is shown in Chapter A.2.2, which shows the fvSolution dictionary file.

A.3.1 fvSchemes dictionary

```
/*--------------------------------*- C++ -*----------------------------------*\
| =========                 |                                                 |
| \\      /  F ield         | OpenFOAM: The Open Source CFD Toolbox           |
|  \\    /   O peration     | Version:  1.7.1                                 |
|   \\  /    A nd           | Web:      www.OpenFOAM.com                      |
|    \\/     M anipulation  |                                                 |
\*---------------------------------------------------------------------------*/
FoamFile
{
    version     2.0;
    format      ascii;
    class       dictionary;
    location    "system";
    object      fvSchemes;
}
// * * * * * * * * * * * * * * * * * * * * * * * * * * * * * * * * * * * * * //

ddtSchemes
{
    default         Euler;
   // default           steadyState;

}

gradSchemes
{
    default         Gauss linear;
    grad(p)         Gauss linear;
    grad(U)         Gauss linear;
}

divSchemes
{
    default         none;
    div(phi,U)      Gauss limitedLinearV 1;
    div((nuEff*dev(T(grad(U))))) Gauss linear;
}

laplacianSchemes
{
    default         none;
    laplacian(nu,U) Gauss linear corrected;
```

```
    laplacian((1|A(U)),p) Gauss linear corrected;
    laplacian(nuEff,U) Gauss linear corrected;

}

interpolationSchemes
{
    default         linear;
    interpolate(HbyA) linear;
    interpolate(U)  linear;
}

snGradSchemes
{
    default         corrected;
}

fluxRequired
{
    default         no;
    p               ;
}



// ************************************************************************* //
```

A.3.2 fvSolution Dictionary

```
/*--------------------------------*- C++ -*----------------------------------*\
| =========                 |                                                 |
| \\      /  F ield         | OpenFOAM: The Open Source CFD Toolbox           |
|  \\    /   O peration     | Version:  1.7.1                                 |
|   \\  /    A nd           | Web:      www.OpenFOAM.com                      |
|    \\/     M anipulation  |                                                 |
\*---------------------------------------------------------------------------*/
FoamFile
{
    version     2.0;
    format      ascii;
    class       dictionary;
    location    "system";
    object      fvSolution;
}
// * * * * * * * * * * * * * * * * * * * * * * * * * * * * * * * * * * * * * //

solvers
```

```
{
    p
    {
        solver          PCG;
        preconditioner  DIC;
        tolerance       1e-09;
        relTol          0;
    }

    U
    {
        solver          PBiCG;
        preconditioner  DILU;
        tolerance       1e-09;
        relTol          0;
    }
}

SIMPLE
{
    nNonOrthogonalCorrectors 0;
    pRefCell        0;
    pRefValue       0;

    residualControl
    {
        p               1e-12;
        U               1e-12;

    }
}

relaxationFactors
{
    fields
    {
        p               0.2;
    }
    equations
    {
        U               0.4;
        nuTilda         0.4;
    }
}


// ************************************************************************* //
```

BIBLIOGRAPHY

1 Sparks, R.S.J., Bursik, M.I., Carey, S.N., Gilbert, J., Glaze, L.S., Sigurdsson, H. and Woods, A. 1997 Volcanic plumes. Wiley.

2 Viskanta, R. 1993 Heat transfer to impinging isothermal gas and flame jets. Experimental Thermal and Fluid Science 6 (3), 111–134.

3 Dec, J. 1997 A conceptual model of DI diesel combustion based on laser-sheet imaging. SAE Technical Paper (970873).

4 Hill, P.G. and Peterson, C.R. 1992 Mechanics and thermodynamics of propulsion (2nd edition). Addison-Wesley Publishing Co.

5 McIlory, H.M., McEligot, D.M, Schultz, R.R., Christensen, D., Pink, R.J. and Johnson, R.C 2006 P.I.V. experiments to measure flow phenomena in a scaled model of a VHTR Lower Plenum. Idaho National Laboratory.

6 Bickley, W.G. 1937 The plane jet. Philosophical Magazine 23 (156), 727–731.

7 Schlichting, Hermann 1968 Boundary-layer theory. pp. 23–51. McGraw-Hill Book Company.

8 Abramovich, G. N. 1963 The theory of turbulent jets. M.I.T. Press.

9 H. M. McIllroy, D. M. McEligot, and R. J. Pink "Measurement of turbulent flow phenomena for the lower plenum of a prismatic gas-cooled reactor," Nuclear Engineering and Design, vol 240, 2010, pp. 416-428.

10 Marsters, G. F. 1977 Interaction of two plane, parallel jets. AIAA Journal 15 (12), 1756–1762.

11 Revuelta, A., Sanchez, A. L. and Linan, A. 2002a Confined axisymmetric laminar jets with large expansion ratios. J. Fluid Mechanics 456, 319–352.

12 Hammad, K.J., Otugen, M.V. and Arik, E.B. 1999 A PIV study of the laminar axisymmetric sudden expansion flow. Experiments in Fluids 26, 266–272.

13 Schlichting, H. 1933 Laminare strahlausbreitung. Journal of Applied Mathematics and Mechanics 13 (4), 260–263.

14 Pai, S. 1954 Fluid dynamics of jets. D. Van Nostrand Company, Inc.

15 Andrade, E. N. and Tsien, L. C. 1937 The velocity distribution in a liquid-into-liquid jet. Proceedings of the Physical Society IV (3), 381–391.

16 Revuelta, A., Sanchez, A. L. and Linan, A. 2002b The virtual origin as a first-order correction for the far-field description of laminar jets. Physics of Fluids 14 (6), 1821–1824.

17 Sarma, A.S.R., Sundararajan, T. and Ramjee, V. 2000 Numerical simulation of confined laminar jet flows. Int. J. Numer. Meth. Fluids 33, 609–626.

18 Iribarne, A., Frantisak, F., Hummel, R. L. and Smith, J. W. 1972 An experimental study of stabilities and other flow properties of a laminar pipe jet. AlChe. Journal 18 (4), 689–698.

19 Back, L. H. and Roschke, E.J. 1972 Shear-layer flow regimes and wave instabilities and reattachment lengths downstream of an abrupt circular channel expansion. J. Applied Mech. pp. 677–681.

20 Durst, F., Pereira, J.C.F. and Tropea, C. 1993 The plane symmetric sudden-expansion flow at low Reynolds numbers. Journal of Fluid Mechanics 248, 567–581.

21 Armaly, B.F., Durst, F., Pereira, J.C.F. and Schonung, B. 1983 Experimental and theoretical investigation of backward-facing step flow. Journal of Fluid Mechanics 127, 473–496.

22 Alleborn, N., Nandakumar, K., Raszillier, H., and Durst, F. 1997 Further contributions on the two-dimensional flow in a sudden expansion. Journal of Fluid Mechanics 330, 169–188.

23 Acrivos, A. and Schrader, M. 1982 Steady flow in a sudden expansion at high Reynolds numbers. Physics of Fluids 25 (6), 923–930.

24 List, E.J. 1982 Turbulent jets and plumes. Annual Review of Fluid Mechanics 19, 189–212.

25 Ball, C.G., Fellouah, H., and Pollard, A. 2012 The flow field in turbulent round free jets. Progress in Aerospace Sciences 50, 1–26.

26 Kandakure, M. T., Patkar, V. C. and Patwardhan, A. W. 2008 Characteristics of turbulent confined jets. Chemical Engineering and Processing 47, 1234–1245.

27 Hussein, H. J., Capp, S. P, and George, W. K. 1994 Velocity measurements in a high-Reynolds-number, momentum-conserving, axisymmetric, turbulent jet. J. Fluid Mechanics 258, 31–75.

28 Panchapakesan, N. R. and Lumley, J. L. 1993a Turbulence measumrents in axisymmetric jets of air and helium. part 1: Air jet. J. Fluid Mechanics 246, 197–223.

29 Panchapakesan, N. R. and Lumley, J. L. 1993b Turbulence measurements in axisymmetric jets of air and helium. part 2: Helium jet. J. Fluid Mechanics 246, 225–247.

30 Greenshields, C. J., Weller, H. G., Gasparini, L. and Reese, J. M. 2009 Implementation of semi-discrete, non-staggered central schemes in a collocated, polyhedral, finite volume framework, for high-speed viscous flows. Int. J. Numer. Meth. Fluids.

31 Patankar, S.V. and Spalding, D.B. 1972 A calculation procedure for heat, mass, and momentum transfer in three-dimensional parabolic flows. International Journal of Heat and Mass Transfer 15, 1787–1806.

32 Jasak, H. 1996 Error analysis and estimation for the finite volume method with applications to fluid flows. PhD thesis, London Imperial College, London.

33 Currie, I. G. 2003 Fundamental mechanics of fluids. pp. 257–259. CRC Press.

34 Roache, P.J. 1997 Quantification of uncertainty in computational fluid dynamics. Annual Review of Fluid Mechanics 29, 123–160.

35 Celik, Ishmail B., Urmila Ghia, and Patrick J. Roache. 2008. Procedure for estimation and reporting of uncertainty due to discretization in CFD applications. Journal of fluids 130.